

1 **First assessment of Aeolus L2A particle backscatter coefficient
2 retrievals in the Eastern Mediterranean**

3
4 Antonis Gkikas¹, Anna Gialitaki^{1,5,6}, Ioannis Binietoglou¹, Eleni Marinou¹, Maria Tsichla¹, Nikolaos
5 Siomos¹, Peristera Paschou^{1,5}, Anna Kampouri^{1,7}, Kalliopi Artemis Voudouri^{1,5}, Emmanouil
6 Proestakis¹, Maria Mylonaki², Christina-Anna Papanikolaou², Konstantinos Michailidis⁵, Holger
7 Baars³, Anne Grete Straume⁴, Dimitris Balis⁵, Alexandros Papayannis², Tomasso Parrinello⁸ and
8 Vassilis Amiridis¹

9
10 ¹Institute for Astronomy, Astrophysics, Space Applications and Remote Sensing, National Observatory of Athens,
11 Athens, Greece

12 ²Laser Remote Sensing Unit, Department of Physics, National and Technical University of Athens, Athens, Greece

13 ³Leibniz-Institut für Troposphärenforschung e.V., Leipzig, Germany

14 ⁴European Space Agency (ESA/ESTEC), Noordwijk, Netherlands

15 ⁵Laboratory of Atmospheric Physics, Aristotle University of Thessaloniki, Thessaloniki, Greece

16 ⁶Department of Physics and Astronomy, University of Leicester, Leicester, United Kingdom

17 ⁷Department of Meteorology and Climatology, School of Geology, Aristotle University of Thessaloniki,

18 54124 Thessaloniki, Greece

19 ⁸European Space Agency (ESA/ESRIN), Frascati, Italy

20 Corresponding author: Antonis Gkikas (agkikas@noa.gr)

21

22 **Abstract**

23 Since 2018, the Aeolus satellite of the European Space Agency (ESA) acquires wind HLOS
24 (horizontal line-of-sight) profiles throughout the troposphere and up to the lower stratosphere, filling
25 a critical gap of the Global Observing System (GOS). Aeolus, carrying ALADIN (Atmospheric LAsEr
26 Doppler INstrument), the first UV HSRL (High Spectral Resolution Lidar) Doppler lidar ever placed
27 in space, along with wind HLOS profiles provides also vertically resolved optical properties of
28 particulates (aerosols, clouds). The present study focuses on the assessment of Aeolus L2A particulate
29 backscatter coefficient (baseline 2A11), retrieved by the Standard Correct Algorithm (SCA), in the
30 Eastern Mediterranean, a region hosting a variety of aerosol species. Ground-based retrievals
31 acquired by lidar instruments operating in Athens (capital of Greece), Thessaloniki (north Greece)
32 and Antikythera (southwest Greece) serve as reference. All lidar stations provide routine
33 measurements to the PANACEA (PANhellenic infrastructure for Atmospheric Composition and
34 climatE chAnge) network. A set of ancillary data including sunphotometric observations
35 (AERONET), reanalysis products (CAMS, MERRA-2), satellite observations (MSG-SEVIRI,

Deleted: hydrometeors

37 MODIS-Aqua) and backward trajectories modelling (FLEXPART) are utilized towards an optimum
38 characterization of the probed atmospheric conditions under the absence of a classification scheme in
39 Aeolus profiles. First, emphasis is given on the assessment of Aeolus L2A backscatter coefficient
40 under specific aerosol scenarios over the Antikythera island. Due to the misdetection of the cross-
41 polar component of the backscattered lidar signal, Aeolus underestimates the aerosol backscatter
42 coefficient by up to 33% when non-spherical mineral particles are recorded (10th July 2019). A good
43 performance is revealed on 3rd July 2019, when horizontally homogeneous loads of fine spherical
44 particles are confined below 4 km. For other two cases (8th July 2020, 5th August 2020), due to noise
45 issues, the Aeolus performance downgrades in terms of depicting the stratification of aerosol layers
46 composed of particles of different origin. According to the statistical assessment analysis for 43
47 identified cases, it is revealed a poor-to-moderate performance for the unfiltered (aerosols plus
48 clouds) Aeolus profiles which improves substantially when cloud contaminated profiles are excluded
49 from the collocated sample. This improvement is evident at both Aeolus vertical scales (regular, 24
50 bins and mid-bin, 23 bins) and it is justified by the drastic reduction of the bias (from 0.45 Mm⁻¹sr⁻¹
51 to 0.27 Mm⁻¹sr⁻¹ for SCA and from 0.69 Mm⁻¹sr⁻¹ to 0.37 Mm⁻¹sr⁻¹ for SCA mid-bin) and root-mean-
52 square-error (from 2.00 Mm⁻¹sr⁻¹ to 1.65 Mm⁻¹sr⁻¹ for SCA and from 1.88 Mm⁻¹sr⁻¹ to 1.00 Mm⁻¹sr⁻¹
53 for SCA mid-bin) scores. In vertical, the Aeolus performance downgrades at the lowermost bins due
54 to either the contamination from surface signals or the increased noise levels for the aerosol retrievals,
55 Among the three PANACEA stations, the best agreement is found at the remote site of Antikythera
56 with respect to the urban sites of Athens and Thessaloniki. Finally, all key Cal/Val aspects necessary
57 for future relevant studies, the recommendations for a possible Aeolus follow-on mission and an
58 overview of the ongoing related activities are thoroughly discussed.

59 60 1. Introduction

61 Atmospheric aerosols constitute a critical component of the Earth system by acting as a major
62 climatic driver (Charlson et al., 1992; Boucher et al., 2013; Li et al., 2022) whereas upon deposition
63 they can affect terrestrial (Okin et al., 2004) and marine ecosystems (Jickells et al., 2005; Li et al.,
64 2018). It is also well documented that they affect several anthropogenic activities with concomitant
65 economic impacts (Middleton et al., 2018; Kosmopoulos et al., 2018). In addition, aerosols
66 accumulation at large concentrations cause an air quality degradation (Kanakidou et al., 2011) with
67 adverse health effects (Pöschl, 2005; Lelieveld et al., 2015) increasing the mortality rates (Health
68 Effects Institute, 2019; Pye et al., 2021). Therefore, their multifaceted role in multidisciplinary
69 research fields highlights the growing scientific concern in understanding and describing the
70 emission, removal, and transport mechanisms governing airborne particles' life cycle. Due to their

Deleted: different

Deleted: very

Deleted: The level of agreement between spaceborne and ground-based retrievals varies with altitude when aerosol layers, composed

Deleted: , are stratified (8th July 2020, 5th August 2020)

Deleted: 6

Deleted: positive tendency

Formatted: Superscript

Deleted:

Formatted: Superscript

Deleted: In vertical, Aeolus performance downgrades at the lowermost bins (attributed to either the surface reflectance or the increased noise levels for the Aeolus retrievals and to the overlap issues for the ground-based profiles).

Deleted: the

Deleted: of aerosols

Deleted: s

Deleted: of air quality

Deleted: that can

Deleted: e

90 pronounced heterogeneity, aerosol burden exhibits a remarkable spatiotemporal variability thus
91 imposing deficiencies in depicting adequately its features and constraints towards a robust assessment
92 of the induced impacts.

Deleted: adequately

93 Passive satellite sensors, providing columnar retrievals of aerosol optical depth (AOD), have
94 been able to reproduce adequately aerosol loads across various spatiotemporal scales. This has been
95 justified via the assessment of AOD versus corresponding sun-photometric measurements (e.g., Wei
96 et al., 2019). Nevertheless, the main drawback arises from the sensors' inability to provide
97 information in vertical. Therefore, this deficiency hampers a reliable quantification of the suspended
98 particles' load within the planetary boundary layer (PBL), related to health impacts. Moreover, it is
99 not feasible to depict the three-dimensional structure of transported loads in the free troposphere,
100 linked to aerosol-cloud-radiation interactions and associated impacts on atmospheric dynamics (Pérez
101 et al., 2006; Gkikas et al., 2018; Haywood et al., 2021). Likewise, passive aerosol observations are
102 not suitable for monitoring stratospheric long-lived plumes that affect aerosol-chemistry interactions
103 and perturb the radiation fields (Solomon et al., 2022). On the contrary, ground-based lidars, relying
104 on active remote sensing techniques, obtain vertical profiles of aerosol optical properties at high
105 vertical and temporal resolution, through multi-wavelength and polarization measurements. Such
106 observations are performed either at networks distributed across Europe (EARLINET; Papalardo et
107 al., 2014; PollyNET; Baars et al., 2016; Engelmann et al., 2016), United States (MPLNET; Campbell
108 et al., 2002), Asia (AD-NET; Sugimoto et al., 2014) and South America (LALINET; Guerrero-
109 Rascado et al., 2016), or at dedicated experimental campaigns (Ansmann et al., 2011; Weinzierl et
110 al., 2016) or even at open seas (Bohlmann et al., 2018). The reproduction of aerosols' vertical
111 structure at global (Liu et al., 2008) and regional (Marinou et al., 2017; Proestakis et al., 2018) scales
112 has been realized through the utilization of measurements acquired by the Cloud-Aerosol Lidar and
113 Infrared Pathfinder Satellite Observation (CALIOP; Winker et al., 2009) and the Cloud-Aerosol
114 Transport System (CATS; McGill et al., 2015; Lee et al., 2019) mounted on the CALIPSO (Cloud-
115 Aerosol Lidar and Infrared Pathfinder Satellite Observation) satellite and the International Space
116 Station (ISS), respectively.

117 On 22nd August 2018, the European Space Agency (ESA) launched its Earth Explorer wind
118 mission, Aeolus, which was a major step forward for Earth Observations (EO) and atmospheric
119 sciences. The Aeolus satellite carries ALADIN (Atmospheric LAser Doppler INstrument), the first
120 space-based high spectral resolution (HSRL) Doppler wind lidar worldwide. ALADIN emits a linear
121 polarized beam which after going through a quarter-wave plate is transmitted with a circular
122 polarization (at 355 nm) and receives the co-polarized backscatter from molecules and
123 particles/hydrometeors in two separate channels (Ansmann et al., 2007; Flamant et al., 2008). The

Deleted: ' features a

Deleted: as it

Deleted: on the vertical distribution of aerosols within the atmosphere

Deleted: T

Deleted: .

Deleted: reproduction

Deleted: e

Deleted: ;

Deleted: as well as to

Deleted: ing

Deleted: ing

Deleted: vertical

Deleted: , as well as the geometric features of the particles' layers

Deleted: .

Deleted: It is

Deleted: Doppler Wind lidar

Deleted: , and was a major step forward for Earth Observations (EO) and atmospheric sciences

145 main mission product is profiles of the horizontally projected line-of-sight winds, and spin-off
146 products are the backscatter and extinction coefficient profiles from particles and hydrometeors. The
147 key scientific objective of Aeolus is to improve numerical weather forecasts and our understanding
148 of atmospheric dynamics and their impacts on climate (Stoffelen et al., 2005; Isaksen and Rennie,
149 2019; Rennie and Isaksen, 2019). After about 1.5 years of instrument and algorithm improvements,
150 the Aeolus L2B wind product was of such good quality (e.g., Witschas et al., 2020; Lux et al., 2020;
151 Martin et al., 2021) that the European Centre for Medium Range Forecasts (ECMWF) could start
152 operational assimilation (January 2020). In May 2020, three further European weather forecast
153 institutes (DWD, Météo-France and the UK MetOffice) started the operational assimilation of Aeolus
154 winds. All meteorological institutes reported that Aeolus winds had significant positive impact on the
155 short and medium term forecasts. The most beneficial impact is found in remote areas (Tropics, S.
156 Hemisphere, polar regions) less covered by other direct wind observations (e.g. ECMWF 2020;
157 Rennie et al., 2021).

158 A series of errors induced by the instrument, by the retrieval algorithm, or by the type of
159 scatterers probed by ALADIN can affect the product quality. It is therefore necessary to perform
160 extensive calibration and validation (Cal/Val) studies utilizing independent reference measurements
161 (e.g. ground-based, aircraft). This task has been performed by the Aeolus Cal/Val community,
162 responding to the Aeolus Announcement of Opportunity to perform product calibration and
163 validation. Such critical tasks are prerequisites to the acceptance of the Mission as “fit for purpose”
164 as it is underlined in the Aeolus Implementation Cal/Val Plan. In contrast to Aeolus wind retrievals,
165 a limited number of studies are focused on the quality of the L2A optical properties. Abril-Gago et
166 al. (2022) performed a statistical validation versus ground-based observations from three Iberian
167 ACTRIS/EARLINET lidar stations affected mainly by dust and continental/anthropogenic aerosols.
168 In their Cal/Val study, they processed AERONET optical properties related to particles' size and
169 nature along with HYSPLIT air-mass backtrajectories towards characterizing the prevailing aerosol
170 conditions. Baars et al. (2021) reported an excellent agreement between Aeolus and Polly^{XT} particle
171 backscatter profiles and adequate agreement of extinction and lidar ratio profiles, between 4 and 12
172 km, for a case of long-range transport of wildfire smoke particles from California to Leipzig
173 (Germany).

174 Here we focus on the comparison of Aeolus L2A particle backscatter coefficient profiles
175 against ground-based profile observations acquired at three lidar stations (Antikythera, Athens,
176 Thessaloniki) contributing to the Greek National Research Infrastructure (RI) PANACEA, an
177 ACTRIS component (<https://www.actris.eu>). All stations are located in the Eastern Mediterranean, a

Deleted: to improve

Deleted: associated

Deleted: The first Aeolus wind product assessment, by the Aeolus Data Innovation Science Cluster (DISC) and Cal/Val teams (e.g. Baars, et al., 2020; Lux et al., 2020; Witschas et al., 2020, ESA 2019), during the instrument commissioning phase in autumn 2018 demonstrated that Aeolus could provide physically meaningful winds in near-real-time immediately after the instrument switch-on in September 2018, demonstrating the space-based Doppler wind lidar principle for the first time. However, the analyses also revealed issues with ALADIN's instrument performance and on-ground data processing performance which needed to be mitigated through careful instrument characterization, instrument adjustments, improved data calibration and on-ground data processor updates.

Deleted: the L2B wind product could therefore be publicly released, which lead to

Deleted:

Deleted: ing

Deleted: to Deutsche Wetter Dienst (DWD), Météo-France and the UK MetOffice

Deleted: found

Deleted: .

Deleted: with the

Deleted: largest

Deleted: in

Deleted: including the tropics, southern hemisphere and polar areas

Deleted: The Aeolus Aladin instrument is a high spectral resolution Doppler wind lidar (HSRL), emitting circularly polarized laser light at 355 nm and observing the co-polarized backscatter from molecules and particles and hydrometeors in two separate channels (Ansman et al., 2007; Flamant et al., 2008). The backscattered light from the surface or top of optically thick clouds up to 30 km altitude is sampled with a vertical resolution of 24 range bins with a thickness from 250 m up to 2 km. The main mission product is profiles of the horizontally projected line-of-sight winds, and spin-off products are the backscatter and extinction coefficient profiles from particles and hydrometeors. In contrast to CALIOP and CATS, ALADIN can retrieve these products without requiring an a priori assumption of the lidar ratio (S), which is characterized by a remarkable variability among aerosol types due to its dependency on particles' shape, composition and size distribution (Müller et al., 2007). However, Aeolus only measures the co-polar part of the atmospheric backscatter and at a single wavelength. Therefore, it is very challenging to discriminate the

Deleted: Aladin

Deleted: continuous and

Deleted: a very limited number of

Deleted:

Deleted:

Deleted: The current study

Deleted: es

Deleted: , that assures a homogenous quality

257 crossroad of air masses (Lelieveld et al., 2002) carrying particles of different nature. The broader
258 Greek area encompasses a variety of aerosol species consisting of: (i) pollutants from industrialized
259 European regions (Gerasopoulos et al., 2003; 2009), (ii) dust aerosols from the nearby deserts (Balis
260 et al., 2004; Papayannis et al., 2005; Gkikas et al., 2016, Marinou et al., 2017), (iii) anthropogenic
261 aerosols from urban areas and megacities (Kanakidou et al., 2011), (iv) biomass burning particles
262 originating in the eastern Europe and the Black Sea (Amiridis et al., 2009; 2010; 2012), (v) smoke
263 aerosols subjected to transport at planetary scale (Baars et al., 2019; Gialitaki et al., 2020), (vi) sea-
264 salt particles produced by bursting bubbles during whitecap formation attributed to wind-wave
265 interactions (e.g. Varlas et al., 2021), (vii) biogenic particles such as airborne fungi and pollen grains
266 (Richardson et al., 2019) and (viii) volcanic ash mixed with sulfate aerosols ejected at high altitudes
267 from explosive Etna eruptions (Zerefos et al., 2006, Kampouri et al., 2021).

Deleted: e.g.

268 The manuscript is structured as follows. In Section 2, a brief overview of the Aeolus satellite
269 and the ALADIN instrument is given. The key elements of the Standard Correct Algorithm (SCA)
270 are summarized in Section 3. The technical information of the ground-based lidars as well as the
271 description of aerosols' regime, in the surrounding area of the PANACEA stations, are presented in
272 Section 4. The collocation criteria between ground-based and spaceborne profiles are described in
273 Section 5. The assessment of Aeolus L2A product under various aerosol scenarios and for the whole
274 collocated sample are discussed in Section 6. The Cal/Val aspects, the recommendations for future
275 relevant studies and the necessary upgrades on ALADIN observational capabilities and Aeolus L2A
276 data content are highlighted in Section 7. Finally, the main findings and the conclusions are drawn in
277 Section 8.

Deleted: aspects

Deleted: and

Deleted: the

Deleted: of aerosol loads

278

279 2. AEOLUS - ALADIN

280

281 A brief description of Aeolus' orbital features, ALADIN's observational geometry and its
282 measurement configuration is given in the current section. This short introduction serves as the
283 starting point for the reader to be familiar with Aeolus' nomenclature. Further details and a more
284 comprehensive overview of the Aeolus satellite mission can be found at ESA technical reports (ESA,
285 1999; 2008; 2016) and at recently published studies (e.g., Lux et al., 2020; Witschas et al., 2022; Lux
286 et al., 2022).

287 ESA's Aeolus satellite, named by the 'keeper of winds' according to the Greek mythology
288 (Ingmann and Straume, 2016), flies in a polar sun-synchronous orbit circling the Earth at an altitude

294 of 320 km with a repeat cycle of 7 days (Kanitz et al., 2019a; Straume et al., 2019). The orbital plane
295 forms an angle of 97° with the equatorial plane, the ground track velocity is about 7.2 km/sec and a
296 complete circle around the Earth takes about 90 minutes for each orbit (Lux et al., 2020; Witschas et
297 al., 2020; Straume et al., 2020). Aeolus is flying over the terminator between day and night
298 (dawn/dusk orbits), with its solar panels facing towards the sun direction for minimizing the solar
299 background illumination (Kanitz et al., 2019).

300 ALADIN, the single payload on the Aeolus satellite platform, is an HSRL lidar (Shipley et
301 al., 1983) equipped with a Nd-YAG laser that emits short laser pulses (~40 to 70 mJ, Witchas et al.,
302 2020) of a circular polarized light at ~355 nm with a 50.5 Hz repetition frequency. The photons that
303 are backscattered from molecules and particulates (aerosols, cloud droplets and ice crystals) at
304 atmospheric altitudes lower than 30 km are collected by a Cassegrain telescope of 1.5 m diameter.
305 The collected photons are directed to the Mie optical channel (Fizeau interferometer) for the analysis
306 of the Doppler shift induced by particulates while the molecular return signals (Rayleigh) are analyzed
307 in two sequentially coupled Fabry-Pérot interferometers (Witchas et al., 2020).

308 ALADIN provides wind and particulate vertically resolved retrievals along the Line-Of-Sight
309 (LOS) by pointing the Earth at a slant angle of 35° off-nadir (see Figure 1 in Flament et al., (2021))
310 which corresponds to an angle of about 37.6° with the Earth surface, due to its curvature. In contrast
311 to CALIOP and CATS, ALADIN can retrieve particulate optical products without requiring an a
312 priori assumption of the lidar ratio (S), which is characterized by a remarkable variability among
313 aerosol types due to its dependency on particles' shape, composition and size distribution (Müller et
314 al., 2007). However, ALADIN only measures the co-polar part of the atmospheric backscatter and at
315 a single wavelength. Therefore, it is very challenging the discrimination between aerosols and clouds
316 and to distinguish further among their subtypes.

317 The instrument detector design allows the sampling of the atmospheric backscatter in 24
318 vertical bins, with a varying resolution from 0.25 (near surface) to 2 km (upper atmosphere). The
319 laser pulses are integrated on-board the satellite along the satellite flight direction, to yield
320 measurements of ~3 km resolution (integration of ~20 laser pulses). During the on-ground data
321 processing, the measurements are accumulated further to yield an "observation" (also called a *Basic*
322 *Repeat Cycle (BRC)*), which corresponds to a distance of ~90 km. The L2A optical properties product
323 which will be described in the next section, derived by the so-called Standard Correct Algorithm
324 (SCA) (Flament et al., 2021), are provided at the observation scale (on a horizontal resolution of ~90
325 km) and are available through the Aeolus Online Dissemination System (<https://aeolus-ds.eo.esa.int>).
326

327 3. Standard Correct Algorithm (SCA)

336 In the current Cal/Val study, we are assessing the performance of the Aeolus L2A particulate
337 products derived by the Standard Correct Algorithm (SCA). Here, we are providing a short overview
338 of the SCA whereas its complete description is available in the Algorithm Theoretical Baseline
339 Document (ATBD; Flamant et al., 2021). The SCA product is derived from the measured signals in
340 the Mie and Rayleigh channels, which are dependent on the instrument calibration constants (K_{ray},
341 K_{mie}), the channel cross-talk coefficients C₁, C₂, C₃ and C₄, the laser pulse energy (E₀) and the
342 contributions from the pure molecular (X) and particulate (Y) signals (see Equations 1 and 2 in
343 Flament et al. (2021)). The latter ones, at each bin, result from the vertical integration of the
344 backscatter (either molecular or particulate) where the squared one-way transmission through the
345 atmosphere is taken into account (see Equations 3 and 4 in Flament et al. (2021)).

346 The separation of the molecular and particle signals on each channel is imperfect, due to the
347 HSRL instrument design, which makes necessary a cross-talk correction. The channel cross-talk
348 corresponding to the transmission of the Rayleigh-Brillouin spectrum (depending on the temperature,
349 pressure and the Doppler shift) through the Rayleigh and Mie channels is expressed by the calibration
350 coefficients C₁ and C₄, respectively (Flament et al., 2021). The other two coefficients, C₂ and C₃,
351 refer to the transmission of a Mie spectrum (depending on the Doppler shift) through the Mie and
352 Rayleigh channels, respectively. Along with the cross-talk coefficients, the instrument calibration
353 constants (K_{ray}, K_{mie}) (see in Flament et al., 2021) are included in the AUX_CAL files.

354 Finally, the cross-talk corrected signals, normalized with the range bin thickness and corrected
355 by the range between the satellite and the observed target, are utilized for the retrieval of the vertically
356 resolved backscatter (β) and extinction (α) coefficients. The former, at each bin, is derived by the Y/X
357 ratio multiplied with the molecular backscatter coefficient (see Equations 9 and 10 in Flament et al.,
358 2021) computed from the pressure and temperature ECMWF simulated fields according to Collis and
359 Russel (1976). For the L2A extinction retrievals, derived via an iterative process from top to bottom,
360 the normalized integrated two-way transmission (NITWT) is applied, using measured and simulated
361 pure molecular signals, under the assumption that the particles' extinction at the top-most bin is zero
362 (see equations 11-14 in Flament et al., 2021). This consideration makes the downwards solution of
363 the integral equations quite sensitive to the noise within the topmost bin (at altitudes ~20-25 km),
364 which is used as reference for the normalization, particularly under low SNR conditions due to the
365 low molecular density. This is a challenge frequently faced for the Aeolus observations due to the
366 weaker measured signals than those of the pre-launch expectations (Reitebuch et al., 2020) as well as
367 to the possible presence of stratospheric aerosols within the top-most range bin or above. In principle,
368 the extinction is retrieved recursively taking into account the attenuation from the overlying bins and
369 by contrasting observed and simulated molecular signals. By differentiating two consecutive bins,

Deleted: are

Deleted: three retrieval algorithms, namely

Deleted: , the Mie Correct Algorithm (MCA) and the Iterative Correct Algorithm (ICA) and their full description is provided

Deleted: MCA relies only on the Mie channel returns and the implementation of the Klett method (Klett, 1981) under the assumption of a universal lidar ratio (~14 sr). On the other hand, ICA works under the assumption of different partial filling of the particles within the range bin. Finally, there is also the *group* product in which signals of high signal-to-noise (SNR) ratio are accumulated prior to the implementation of the SCA algorithm. Both ICA and group products are still under development and they are not recommended to be utilized in scientific studies (Flament et al., 2021). ¶ Among the aforementioned Aeolus L2A retrieval algorithms, the primary, the most reliable and mature is the SCA.

Deleted: o

Deleted: for

Deleted: "C

Deleted: "

Deleted: a method called

Deleted: "

Deleted: "

395 unrealistically high positive or negative extinctions can be retrieved (see Fig. 10 in Flament et al.,
396 (2021)) resulting from fluctuations between strong and weak attenuation.

397 In the case of negative extinction values, the SCA algorithm regularizes the solution by
398 resetting to zero (Flament et al., 2021), which can lead to an underestimation of the partial column
399 transmission. In order to compensate the impacts of the aforementioned issues, it has been shown by
400 error propagation calculations (see equations 18 and 19 in Flament et al. (2021)), that averaging two
401 consecutive bins the retrieved extinction becomes more reliable at the expense of the vertical
402 resolution (23 bins; “mid-bin” vertical scale). In contrast to SCA, in the SCA mid-bin negative
403 extinction values can be found since the zero-flooring constraint is not implemented. For consistency
404 reasons, the averaging between two neighboring bins is applied also in the backscatter coefficient
405 thus allowing the derivation of the lidar ratio.

Deleted:

406 The inherent weaknesses of the SCA algorithm have been mitigated in the Maximum
407 Likelihood Estimation (MLE) algorithm (Ehlers et al., 2022). Its main principle relies on the
408 exploitation of all available information and the definition of constraints on the positivity of the
409 retrieved optical properties and on the expected range of the lidar ratio. Under these restrictions, the
410 particle extinction is derived when the particle backscatter is available and vice versa. According to
411 the evaluation versus ground-based observations and SCA end-to-end simulated optical products, it
412 is revealed a remarkable improvement (up to one order) on the precision of the extinction and the
413 lidar ratio due to effective noise dampening. Moreover, there is also a beneficial impact on the co-
414 polar backscatter coefficient. Another new algorithm that outperforms SCA is the AEL algorithm
415 (adjusted from the EarthCARE-ATLID algorithms) providing a feature mask (AEL-FM) at the
416 highest available resolution and aerosol/clouds extinction and lidar ratios via a multi-scale optimal
417 estimation method (AEL-PRO). Both MLE and AEL retrievals have been released at a more recent
418 baseline (2A14) than those used in the current study (2A11) and for this reason are omitted from our
419 Cal/Val analysis.

420

421 **4. Ground-based lidars (PANACEA)**

422 The ground-based observational datasets used herein, are taken from stations contributing to
423 the PANhellenic infrastructure for Atmospheric Composition and climatE chAnge (PANACEA)
424 initiative. Within PANACEA, different measurement techniques and sensors are utilized in a
425 synergistic way for monitoring the atmospheric composition and climate change related parameters
426 in Greece.

427 The locations of the stations providing routine measurements to the PANACEA network are
428 shown in Figure 1-i. For the assessment analysis of Aeolus L2A products, we utilize available

Deleted: In the case of negative extinctions, the SCA algorithm regularizes the solution by resetting extinction to zero (Ehlers et al., 2022), which can lead to an underestimation of the partial column transmission. In order to compensate the impacts of the aforementioned issues, it has been shown by error propagation calculations (see equations 18 and 19 in Flament et al. (2021)), that by averaging two consecutive bins the retrieved extinction becomes more reliable at the expense of the vertical resolution (23 bins; “mid-bin” vertical scale). In contrast to SCA, in the SCA mid-bin negative extinctions can be found since the zero-flooring constraint is not implemented. For consistency reasons, the averaging between two neighboring bins is applied also in the backscatter coefficient thus allowing the derivation of the lidar ratio. ¶

Deleted: that participate

Deleted: in

Deleted: adverse

448 measurements from PANACEA stations, namely Antikythera (ANT), Athens (ATH) and
449 Thessaloniki (THE), equipped with multiwavelength polarization lidar systems. All stations comply
450 with the quality-assurance criteria established within EARLINET (e.g. see Freudenthaler et al., 2016)
451 so as to assure the provision of high-quality aerosol related products. Consequently, the derived
452 datasets can be considered for any validation purpose. To ensure the homogeneity, and the consistency
453 of the optical property profiles derived from the adverse lidar systems operating at each station, the
454 Single Calculus Chain algorithm (SCC; D' Amico et al., 2016; Mattis et al., 2016) was used; an
455 automatic processing chain for lidar data, developed within EARLINET. All systems employ multiple
456 detectors, operating either in the photon-counting or analog mode. Herein elastically and inelastically
457 backscattered signals at 355 and 387 nm, were used to evaluate Aeolus products. The optical property
458 profiles were derived using the Raman and Klett-Fernald-Sassano inversion methods (Ansmann et al.
459 1992; Fernald, 1984; Klett, 1981; Sasano and Nakame, 1984) during night-time and daytime
460 measurements respectively. ▾

461

462 4.1 Antikythera

463 Regular lidar measurements have been performed at the PANGEA observatory (PANhellenic
464 GEophysical observatory of Antikythera; lat=35.86° N, lon=23.31° E, alt=193 m asl.) contributing to
465 this study. The lidar system deployed at PANGEA is operated by the National Observatory of Athens
466 (NOA). It is a Polly^{XT} (Engelmann et al., 2016) multi-wavelength Polarization-Raman-Water vapor
467 lidar, designed for unattended, continuous operation. Polly^{XT} deploys an Nd:YAG laser which emits
468 linearly polarized light at 355, 532 and 1064 nm. The radiation elastically and inelastically
469 backscattered from aerosol, cloud particles, nitrogen (at 387 and 607 nm) and water vapor (at 407
470 nm) molecules, is collected using a near-range (spherical mirror of 50 mm diameter, focal length
471 f=250 mm and 2.2 mrad field of view (FOV)) and a far-range receiver (Newtonian telescope with a
472 300 mm diameter primary mirror, f=900 m and 1 mrad FOV) at a raw vertical resolution of 7.5m.
473 The combined use of the near-range and far-range receivers allows for the retrieval of the aerosol
474 optical properties from 500 m up to ~12-14 km above the ground. A detailed description of the
475 technical characteristics of Polly^{XT} can be found in Engelmann et al. (2016).
476

477 4.2 Athens

478 The Laser Remote Sensing Unit of the National and Technical University of Athens, Greece
479 (LRSU; NTUA; lat=37.96° N, lon=23.78° E, alt=200 m asl.), is part of the EARLINET since May
480 2000. Currently, the Athens lidar station performs simultaneous measurements with two different
481 lidar systems, EOLE and DEPOLE. The EOLE lidar is an advanced 6-wavelength elastic

Formatted: English (United States)

Deleted: in

Deleted: Below the full overlap height and under the assumption of a well-mixed boundary layer, lidar profiles can be linearly extended to the ground (Siomos et al., 2018, Baars et al., 2016).

Deleted: Under the prevailing Mediterranean background conditions, and being across the traveled path of different air masses (i.e. marine particles, Saharan dust), Antikythera is considered as an ideal location for Cal/Val activities.¶

Deleted:

492 backscatter/Raman lidar system able to provide the aerosol backscatter coefficient at 355, 532 and
493 1064 nm, the aerosol extinction coefficient at 355 and 532 nm and water vapor mixing ratio profiles
494 in the troposphere. EOLE is based on a pulsed Nd:YAG laser system and a 300 mm diameter
495 receiving Cassegrain telescope (f=600 mm, FOV =1.5 mrad) which collects all elastically
496 backscattered lidar signals (355-532-1064 nm), as well as generated by the vibrational Raman effect
497 (by atmospheric N₂ at 387-607 nm and by H₂O at 407 nm). The full overlap (i.e. the altitude from
498 which upwards the whole lidar beam is within the telescope FOV) of EOLE is reached at,
499 approximately, 812 m a.s.l.. EOLE has been validated within EARLINET at hardware level by two
500 intercomparison campaigns (Matthias et al., 2004), in order to fulfill the standardized criteria.

Deleted: 4

Deleted: those

Deleted: spontaneous

501 The DEPOLE lidar is a depolarization lidar, able to provide profiles of the aerosol backscatter
502 coefficient and the linear particle/volume depolarization ratio at 355 nm. DEPOLE is based on a
503 pulsed Nd:YAG laser system which emits linearly polarized light at 355 nm. The elastically
504 backscattered lidar signals at 355 nm are collected by a 200 m diameter Dall-Kirkham/Cassegrain
505 telescope (f=600 mm, FOV=3.13 mrad) and the full overlap is reached at, approximately, 500 m a.s.l..

Deleted: is

507 4.3 Thessaloniki

508 Thessaloniki's multiwavelength Polarization Raman lidar system (THELISYS) belongs to the
509 Laboratory of Atmospheric Physics that is located at the Physics Department of the Aristotle
510 University of Thessaloniki (lat = 40.63° N, lon = 22.96° E, a.s.l. = 50m). Thessaloniki is a member
511 station of the EARLINET since 2000, providing almost continuous measurements, according to the
512 network schedule (every Monday morning, ideally close to 12:00 UTC, and every Monday and
513 Thursday evening) and during extreme events (e.g., Saharan dust outbreaks, smoke transport from
514 biomass burning, volcanic eruptions) and satellite overpasses. THELISYS has been validated within
515 EARLINET at hardware level by two intercomparison campaigns (Matthias et al., 2004), in order to
516 fulfill the standardized criteria. The system is based on the first (1064 nm), second (532 nm), and
517 third harmonic (355 nm) frequency of a compact, pulsed Nd:YAG laser emitted with a 10 Hz
518 repetition rate. THELISYS setup includes three elastic backscatter channels at 355, 532 and 1064nm,
519 two nitrogen Raman channels at 387 nm and 607nm, and two polarization sensitive channels at 532
520 nm. The acquisition system is based on a LICEL Transient Digitizer working in both the analogue
521 and photon counting (250 MHz) mode. The vertical resolution of the elastic raw signal at 355 nm is
522 equal to 3.75 m and is recorded in both analog and photon counting mode. The full overlap height is
523 almost 800m a.s.l. A detailed description of THELISYS can be found in Siomos et al. (2018) and
524 Voudouri et al. (2020).

Deleted: in

Deleted: I

Deleted: I

533 4.4. Aerosols' load variability in the vicinity of the PANACEA sites

534 The variability of the atmospheric aerosol load in the vicinity of three PANACEA stations
535 (Fig. 1-i) is discussed in this section. The aim of this introductory analysis is to investigate the
536 horizontal homogeneity of the aerosol optical depth (AOD) in the respective broader areas, playing a
537 key role in the comparison of ground-based and spaceborne profiles, which are not spatially
538 coincident as it will be shown in [Section 5](#). For the purposes of this analysis, we have processed the
539 mid-visible (550 nm) [columnar](#) AOD retrievals, over the period 2008-2017, acquired by the MODIS
540 sensor, mounted on the Aqua polar orbiting satellite. More specifically, we have analyzed the Level
541 2 (L2; [swaths; 5-min segments](#)) MODIS-Aqua AODs, obtained by the latest version (Collection 6.1)
542 of the operational retrieval algorithms (Remer et al., 2008; Levy et al., 2013; Sayer et al., 2013). [The](#)
543 [aforementioned data are](#) accessible [via](#) the Level 1 and Atmosphere Archive and Distribution System
544 (LAADS) Distributed Active Archive Center (DAAC) (<https://ladsweb.modaps.eosdis.nasa.gov/>, last
545 access: 17 June 2022).

546 For each station, we have calculated the [arithmetic mean of AODs, representative over the](#)
547 [period 2008-2017](#), within progressively larger circular areas, with radii spanning from 10 to 100 km
548 with an incremental step of 10 km (Fig. 1-ii). Figure 1-iii illustrates the resulting AODs for each
549 station (x labels) and at each radius (colored bars). In order to ensure the reliability of the obtained
550 results, only the best (QA=3) MODIS-Aqua AOD L2 retrievals are considered whereas the spatial
551 averages [\(computed individually for each circle\)](#) are calculated only when the satellite observations
552 are simultaneously available at all circles. In the urban areas of Athens (ATH) and Thessaloniki
553 (THE), the contribution of anthropogenic aerosols on the columnar load fades for increasing radii.
554 On the contrary, at Antikythera (ANT), the spatial AOD means remain almost constant revealing a
555 horizontal homogeneity of the aerosol load in the broader area. An alternative way to compare the
556 differences in the AOD spatial representativeness between the urban (ATH, THE) and the remote
557 (ANT) sites [has been performed](#). Fig. 1-iv [illustrates](#) the normalized values for each radius with
558 respect to the AOD levels of the inner circle (i.e., up to 10 km distance from the station). In both
559 urban sites the values are lower than one (dashed line), decreasing steadily in THE and smoothly in
560 ATH after an abrupt reduction from 10 to 20 km. In ANT, the blue curve resides almost on top of the
561 dashed line throughout the circles radii (i.e., range of distances) indicating the absence of significant
562 horizontal variation of the aerosol load suspended in the surrounding area of the station.

563 [A key aspect which has not been adequately addressed in Fig. 1-iii, is the temporal variability](#)
564 [of aerosol loads since the spatiotemporally averaged AODs “hide” such information. A useful](#)
565 [measure for this purpose is the coefficient of variation \(CV\), defined as the ratio of the standard](#)
566 [deviation and the arithmetic mean of AOD \(Anderson et al., 2003; Shinozuka and Redemann, 2011\).](#)

Deleted: a following section (i.e., collocation method)

Deleted: ,

Deleted: from

Deleted: average

Deleted: value

Deleted: is depicted in

Deleted: showing

Deleted: ,

575 [Figure 1-v displays the CV values \(expressed in percentage\), computed for the period 2008-2017, for](#)
576 [each circle at each station. The highest levels \(up to 90%\) are recorded in Antikythera whereas lower](#)
577 [values \(up to 70%\) are recorded in THE and the lowest ones are found in ATH \(up to 60%\). This](#)
578 [discrepancy is mainly attributed to the higher frequency of dust outbreaks affecting the southern parts](#)
579 [of Greece in contrast to the central and northern sectors of the country \(Gkikas et al., 2013; 2016\). It](#)
580 [is noted that all the PANACEA sites are also under the impact of advected loads composed by](#)
581 [anthropogenic/biomass particles originating at distant areas. Nevertheless, their frequency of](#)
582 [occurrence and their concentration is rarer and weaker, respectively, than those of the advected](#)
583 [Saharan dust. Between the remote \(ANT\) and urban \(ATH, THE\) sites there is clear difference of the](#)
584 [CV dependence with respect to the circle radius. In ANT, the CVs increase steadily from the inner to](#)
585 [the outer circle while an opposite tendency is found in THE and ATH. The increasing trend in ANT](#)
586 [is mainly regulated by the range of the Saharan plumes transported towards southwest Greece. On](#)
587 [the contrary, the declining trend revealed in the two main Greek cities indicates that the temporal](#)
588 [variability of the local sources \(i.e., two first cycles\) is more pronounced. For completeness, we have](#)
589 [also computed the spatial autocorrelation \(Anderson et al., 2003; Shinozuka and Redemann, 2011\)](#)
590 [among the averaged AODs of each circle area. The correlation matrices for each station are presented](#)
591 [in Fig. S1. Among the three PANACEA sites, the R values in Athens \(Fig. S1-i\) drop rapidly, with](#)
592 [respect to the first circle \(10 km radius\), highlighting the strong spatial contrast of AODs between the](#)
593 [city and the surrounding areas. For the outer domains, this transition becomes significantly smoother](#)
594 [and the R values are higher than 0.90 in most of the combinations indicating a spatial coherence. In](#)
595 [Thessaloniki \(Fig. S1-iii\), the pattern of the R values onto the correlation matrix is similar with those](#)
596 [of Athens but the high R values \(> 0.89\) indicate a better spatial AOD homogeneity according to](#)
597 [Anderson et al. \(2003\). Finally, under the absence of local sources in Antikythera and strong](#)
598 [horizontal AOD variability in the vicinity, the computed R value between the inner \(10 km radius\)](#)
599 [and the outer \(100 km radius\) circle is higher than 0.94 and increases at shorter distances.](#)

600 601 **5. Collocation between Aeolus and ground-based lidars**

602 The assessment of Aeolus L2A backscatter profiles has been performed against the
603 corresponding measurements acquired at the three EARLINET/PANACEA lidar stations. In Figure
604 2, three examples of the collocation between ground-based and spaceborne retrievals are illustrated
605 in order to describe our approach as well as to clarify points needed in the discussion of the evaluation
606 results (Section 6). At each station, we identify the observations (BRCs), considering their
607 coordinates at the beginning of the ALADIN scan, falling within a circle of 120 km radius (black
608 dashed circle) centered at the station coordinates (black dot). Based on the defined spatial criterion,
609 [applied for each case,](#) the number of BRCs residing within the 120 km circle should be at least one

610 and cannot be more than three. We denote each one of them, along the ALADIN measurement track
611 (white stripe), with different colors (red, blue and magenta) in Fig. 2. The green arrow shows the
612 flight direction of the satellite for the dusk (ascending) or dawn (descending) orbits. For the ground-
613 based observations, the aerosol backscatter profiles are derived considering a time window of ± 1
614 hour around the satellite overpass. Nevertheless, this temporal collocation criterion has been relaxed
615 or shifted in few cases to improve the quality of the ground-based retrievals (i.e., by increasing the
616 signal-to-noise ratio) as well as to increase the matched pairs with Aeolus L2A profiles. Both
617 compromises are applied since the weather conditions favoring the development of persistent clouds
618 may eliminate the number of simultaneous cases. It is noted, however, when the temporal window is
619 shifted or relaxed we are taking into account the homogeneity of the atmospheric scene (probed by
620 the ground lidar). For the Antikythera station we did not deviate from the pre-defined temporal
621 criterion apart from one case study. In Thessaloniki and Athens, the time departure between Aeolus
622 and ground-based profiles can vary from 1.5 to 2.5 hours. Overall, 43 cases are analyzed out of which
623 15 have been identified over Antikythera, 12 in Athens and the remaining 16 in Thessaloniki.

Deleted: orange

Formatted: Font: (Default) Times New Roman, 12 pt

Deleted:

Formatted: Font: (Default) Times New Roman, 12 pt

Deleted: 6

Deleted: rest

624 The ground-based profiles are derived under cloud free conditions in contrast to Aeolus L2A
625 backscatter profiles providing aerosol and/or cloud backscatter. Therefore, a cloud screening of the
626 Aeolus data using auxiliary cloud information was applied. In the framework of the present study, the
627 exclusion of cloud contaminated Aeolus profiles relies on the joint processing of the cloud mask
628 product (CLM; <https://www.eumetsat.int/media/38993>; CLOUD MASK PRODUCT
629 GENERATION) derived from radiances acquired by the SEVIRI (Spinning Enhanced Visible and
630 Infrared Imager) instrument mounted on the Meteosat Second Generation (MSG4) geostationary
631 satellite (Schmetz et al., 2002). It should be noted, however, that the CLM product serves as an
632 indication of clouds presence, without providing information about their macrophysical properties
633 (i.e., cloud coverage), their phase (i.e., ice, water, mixed) or their categories (i.e., low, middle, high).
634 According to the product user guide (https://www-cdn.eumetsat.int/files/2020-04/pdf_clm_pg.pdf;
635 Section 3.4), artificial straight lines can be found because the ECMWF temperature/humidity fields
636 are not interpolated in time and space. Moreover, due to the limited number of levels of ECMWF
637 temperature profiles, required for the atmospheric correction, the cloud detection in the lower
638 troposphere is impacted. Finally, broken clouds with limited spatial extension as well as thin cirrus
639 are likely misdetected by MSG. In the illustration examples of Figure 2, the grey shaded areas
640 represent the CLM spatial coverage at each PANACEA site. Based on the filtering procedures, the
641 Aeolus L2A backscatter retrievals, throughout the probed atmosphere by ALADIN, are removed from
642 the analysis when the grey shaded areas overlap with a BRC.

Deleted: by

Deleted: of CLM in the broader area a

643 6. Results

651 6.1 Assessment of Aeolus L2A backscatter under different aerosol scenarios

652 In the first part of the analysis we assess the quality of the Aeolus L2A backscatter under
653 various aerosol regimes aiming to: (i) investigate the capabilities of the ALADIN spaceborne lidar to
654 detect aerosol layers, (ii) investigate how the horizontal homogeneity and vertical structure of the
655 aerosol layers can affect the level of agreement between spaceborne and ground-based retrievals and
656 (iii) demonstrate the synergistic use of various datasets for a better characterization of the prevailing
657 aerosol conditions. All of these aspects are necessary towards a comprehensive Cal/Val study to
658 facilitate the interpretation of our findings and to identify possible upgrades on Aeolus retrievals.
659 Overall, four cases over the Antikythera island (southwest Greece) are analyzed for the Aeolus L2A
660 aerosol backscatter retrievals (Baseline 2A11). The obtained results are depicted in Figure 3. The
661 identified cases have been selected because they are representing some of the most typical aerosol
662 conditions in the E. Mediterranean. Note that for each case we are selecting the nearest Aeolus BRC
663 to station coordinates that falls entire within the circle area.

664 As it has been already mentioned, Aeolus retrievals are provided at coarse spatial (BRC level;
665 ~90 km) and vertical (minimum 250 m) resolution, while currently there is no scene classification
666 scheme. In order to overcome this inherent limitation, as much as possible, several ancillary data and
667 products are utilized in parallel with those of the MSG-SEVIRI CLM product. Based on the
668 FLEXPART v10.4 Lagrangian transport model (Stohl et al., 2005; Ignacio Pisso et al., 2019) we have
669 reproduced the 5-day air masses backtrajectories prior to their arrival at 7 altitudes above the ground
670 station. FLEXPART was driven with 3-hourly meteorological data from the National Centers for
671 Environmental Prediction (NCEP) Global Forecast System (GFS) analyses provided at $0.5^\circ \times 0.5^\circ$
672 resolution and for 41 model sigma pressure levels
673 (https://nomads.ncep.noaa.gov/txt_descriptions/GFS_half_degree_doc.shtml). To depict the spatial
674 patterns of the mid-visible (550 nm) total and speciated AOD, we are relying on the MERRA-2
675 (Modern-Era Retrospective analysis for Research and Applications version 2; Buchard et al., 2017;
676 Randles et al., 2017; Gelaro et al., 2017) and CAMS (Copernicus Atmosphere Monitoring Service;
677 Inness et al., 2019) reanalysis datasets, both providing AODs of high quality (Gueymard and Yang,
678 2020; Errera et al., 2021). Finally, AERONET sun-direct measurements (Level 2.0, Version 3; Giles
679 et al., 2019; Sinyuk et al., 2020) of spectral AODs and Ångström exponent as well as the Fine Mode
680 Fraction (FMF at 500nm) derived from the spectral deconvolution algorithm (O'Neill et al., 2003)
681 are also used for the characterization of the aerosol load and size over the station.

683 6.1.1 Dust advection on 10th of July 2019

Deleted: for

Deleted: ing

Deleted: the obtained

Deleted: at a further step for

Deleted: ing

Deleted:

Deleted: and t

Deleted: representative

Deleted: For

Deleted: ing

Deleted: aerosol products

Deleted: 1

Deleted: 5

Deleted: and the temporal evolution

698 The first case refers to the advection of dust aerosols from northwest Africa towards
699 Antikythera with dust-laden air masses crossing southern Italy prior to their arrival from northwest
700 directions (Figure S2). This route of air masses, driven by the prevailing atmospheric circulation
701 (Gkikas et al., 2015), is typical during summer when Saharan aerosols are advected towards the
702 eastern Mediterranean (Balis et al., 2006). MERRA-2 (Fig. S3-i) and CAMS (Fig. S3-ii) show a
703 reduction of AODs (at 550nm) from west to east whereas the large contribution (>80%) of dust
704 aerosols to the total aerosol load is evident in both reanalysis products (results not shown here). The
705 moderate-to-high AOD values are confirmed by the ground-based sunphotometric measurements
706 (Fig. S4) which are associated with low Ångström exponent (calculated between 440 nm and 870
707 nm) values (0.2 – 0.4) and FMF (Fig. S5) lower than 0.35 thus indicating the prevalence of coarse
708 mineral particles (Dubovik et al., 2002). This is further supported from Polly^{XT} measurements (Fig.
709 S6) revealing persistent dust layers associated with volume linear depolarization ratio (VLDR) values
710 of 5-10% at 355 nm, stretched from altitudes close to the ground and up to almost 6 km.

711 This case is suitable for evaluating L2A backscatter retrievals since non-spherical mineral
712 particles are probed by ALADIN, which does not detect the cross-polar component of the
713 backscattered lidar signal. Therefore, a degradation of ALADIN's performance is expected (i.e.,
714 underestimation of the backscatter coefficient and overestimation of the lidar ratio) when aspherical
715 particles (e.g., dust, volcanic ash, cirrus ice crystals) are probed. In Figure 3, the backscatter
716 coefficient step-like vertical profiles from Aeolus at the regular (brown) and mid-bin (black) vertical
717 scales are compared against those acquired by the Polly^{XT} (pink) at 355 nm. The colored dashed lines
718 (Aeolus) and the pink shaded area (Polly^{XT}) correspond to the statistical uncertainty margins of the
719 spaceborne (see Section 2.3.1 in Flament et al., (2021)) and the ground-based (D'Amico et al., 2016)
720 retrievals, respectively. Both refer to the photocounting noise following a Poisson distribution. At a
721 first glance, it is revealed that the geometrical structure of the dust layer, extending from 1 to 6 km,
722 is generally well captured by ALADIN (except at altitude ranges from 1 to 2.5 km), but the
723 backscatter magnitude is constantly underestimated. A fairer comparison requires the conversion of
724 the backscatter retrievals assuming that Polly^{XT} emits circularly polarized radiation (instead of
725 linearly polarized) thus resembling ALADIN. Under the assumption of randomly oriented particles
726 and negligible multiple scattering effects, this transformation is made based on theoretical formulas
727 (Mishchenko and Hovenier, 1995; Roy and Roy, 2008), as it has been shown in Paschou et al. (2021).
728 Following this approach, the Aeolus-like backscatter (i.e., circular co-polar component; blue curve in
729 Fig. 3) is reproduced for the ground-based profiles at altitudes where UV depolarization
730 measurements are available. Thanks to this conversion, the Aeolus-Polly^{XT} negative biases diminish
731 and the Aeolus-like curve resides closer to those of SCA (brown) and SCA mid-bin (black)

Deleted: the
Deleted: island
Deleted: to the PANACEA site
Deleted: 4
Deleted: 3
Deleted: 3

Deleted: 1
Deleted: and

Deleted: 2

Deleted: ideal

Formatted: English (United States)

Deleted: , considering that depolarizing particles are recorded.

Deleted: and

745 backscatter levels. The difference between pink and blue backscatter profiles, ranging from 13 to 33%
746 in this specific case, reflects the underdetermination of the particle backscatter coefficient in case of
747 depolarizing aerosols being probed, due to the missing cross-polar backscatter component.

748

749 6.1.2 Long-range transport of *fine* aerosols on 3rd July 2019

750 Under the prevalence of the Etesian winds (Tyrilis and Lelieveld, 2013), anthropogenic
751 aerosols from megacities (Kanakidou et al., 2011) and biomass burning particles originating in the
752 eastern Europe (van der Werf et al., 2017) are transported southwards. Based on the FLEXPART
753 simulations (Fig. S7), the air masses carrying fine particles, gradually descend till their arrival over
754 Antikythera from north-northeastern directions. During early morning hours, when ALADIN probes
755 the atmosphere at a distance of ~90 km westwards of the ground station (dawn orbit; descending),
756 moderate AODs (up to 0.15 at 340 nm), very high Ångström exponent values (>1.2) and FMFs
757 varying from 0.6 to 0.7 are measured with the Cimel sunphotometer (Fig. S8 and Fig. S9). The aerosol
758 load is confined below 2.5 km consisting of spherical particles as it is revealed from the Polly^{XT}
759 volume linear depolarization ratio (VLDR) values, which do not exceed 5% at 355 nm (Fig. S10). In
760 the vicinity of the PANGEA observatory, MERRA-2 (Fig. S11-i) and CAMS (Fig. S11-ii) AODs,
761 mainly attributed to organic carbon, sulphate and sea-salt aerosols, do not exceed 0.2 and they are
762 coherent in spatial terms (i.e., horizontal homogeneity). In this case, Polly^{XT} particle backscatter
763 coefficient profiles coincide with the corresponding Aeolus-like profiles (pink and blue curves are
764 almost overlaid in Fig. 3-ii) since depolarization values are negligible. Under these conditions,
765 ALADIN is capable of reproducing satisfactorily the layer's structure whereas slightly overestimates
766 its intensity with respect to the ground-truth retrievals.

767

768 6.1.3 Long range transport of *fine* aerosols on 8th July 2020

769 On 8th July 2020, the broader area of the Antikythera island was under the impact of moderate-
770 to-high aerosol loads, mainly consisting of organic and sulphate particles, in the western and southern
771 sector of the station, based on CAMS simulated AODs (up to 0.5) (Fig. S12-ii). AERONET
772 measurements yield UV AODs up to 0.5 and Ångström exponent higher than 1.5 during early
773 afternoon (Fig. S13) whereas the FMF is higher than 0.75 throughout the day (Fig. S14). MERRA-2
774 AOD patterns (Fig. S12-i) and speciation (strong contribution from marine and sulphate aerosols to
775 the total aerosol load) are different from those of CAMS, without being very consistent with respect
776 to the ground-based sunphotometer observations (Fig. S13, Fig. S14). Air masses originating in
777 northern Balkans and the Black Sea, after crossing metropolitan areas (i.e., Istanbul, Athens), are
778 advected over ANT at altitudes up to 4 km above surface. A second cluster aloft (>5 km) indicates

Moved (insertion) [1]

Deleted: particles originating from

Deleted: a typical pattern dominating over the broader Greek area during summer months, when winds blow mainly from N-NE directions,

Moved up [1]: anthropogenic aerosols from megacities (Kanakidou et al., 2011) and particles originating from biomass burning in the eastern Europe and in the surrounding area of the Black Sea (van der Werf et al., 2017) are transported southwards.

Deleted: and in the surrounding area of the Black Sea

Deleted: 8

Deleted: and

Deleted: 5

Deleted: 6

Deleted: 7

Deleted: 7

Deleted: blue

Deleted: pink

Deleted: (SCA retrievals - brown curve)

Deleted: (SCA mid-bin retrievals - black curve)

Deleted: in the western and southern sector of the station

Deleted: 1

Deleted: The prevalence of fine aerosols is confirmed by the

Deleted: ,

Deleted: ing

Deleted: 9

Deleted: 1

Deleted: indicating a moderate performance

Deleted: 9

Deleted: , whereas

Deleted: a

810 the convergence of air masses from northwest (Fig. S15). In vertical terms, aerosol layers with local
811 backscatter maxima gradually reducing from 3.5 to $1.5 \text{ Mm}^{-1} \text{ sr}^{-1}$ are observed up to 4 km based on
812 Polly^{XT} backscatter coefficient profiles (pink curve, Fig. 3-iii) whereas almost identical values are
813 recorded for the Aeolus-like retrievals (blue curve, Fig. 3-iii) under low VLDR levels (Fig. S16). For
814 this specific case, Aeolus' performance reveals an altitude dependency according to the comparison
815 versus Polly^{XT}. From top to bottom, the weak layer extending from 6 to 8 km, observed in the ground-
816 based lidar profiles is partially evident in the Aeolus retrievals. Aeolus erroneously indicates the
817 presence of an aerosol layer between 3 and 4.5 km due to the overlying noise (i.e., negative
818 backscatter coefficients). This deficiency interprets also the underestimation of the backscatter
819 coefficient at altitudes spanning from 2 to 3 km. Below 2 km, the agreement between ALADIN and
820 Polly^{XT} becomes better, particularly for SCA mid-bin, even though the narrow peak recorded at ~ 1.2
821 km by Polly^{XT} cannot be reproduced by ALADIN. This might be attributed either to the adjusted RBS
822 at the lowermost bin (1 km thickness) or to the lower accuracy of Aeolus retrievals near the ground
823 due to the attenuation from the overlying layers (Flament et al., 2021).

Deleted: 2

Deleted:

Deleted: vertically resolved retrievals

Deleted: ,

Deleted: At height ranges ($< 4 \text{ km}$) where the main portion of the aerosol burden resides, there is a contradiction of ALADIN's performance clearly seen beneath and above $\sim 2 \text{ km}$. In the free troposphere, the retrieved backscatter by ALADIN is underestimated with respect to Polly^{XT} retrievals whereas the position of the Aeolus local maximum backscatter ($\sim 1 \text{ Mm}^{-1} \text{ sr}^{-1}$) is recorded exactly above the top of the aerosol layer observed from the ground. On the contrary, below 2 km ,

824

825 6.1.4 Stratification of spherical and non-spherical particles on 5th August 2020

826 In the last case, that took place on 5th August 2020, we are investigating the ability of Aeolus
827 to reproduce adequately the vertical structure of an aerosol layer detected up to 4 km based on Polly^{XT}
828 (Fig. 3-iv; pink curve). The “peculiarity” of this study case, as it is revealed by the Polly^{XT} time-
829 height plots of VLDR (Fig. S17), is that spherical fine particles dominate below 2.5 km whereas the
830 presence of non-spherical coarse aerosols above this layer is evident. This stratification results from
831 the convergence of air masses either originating in central Europe or suspending most of their travel
832 above northwest Africa (Fig. S18). According to MERRA-2 (Fig. S19-i) and CAMS (Fig. S19-ii)
833 reanalysis datasets, AODs fade from west to east while both numerical products indicate the
834 coexistence of carbonaceous, sulphate and mineral particles over the area where ALADIN samples
835 the atmosphere ($\sim 100 \text{ km}$ westwards of Antikythera). During the Aeolus overpass ($\sim 04:40 \text{ UTC}$),
836 sunphotometer columnar observations are not available (Fig. S20, Fig. S21). However, one hour later,
837 UV AODs up to 0.4 are recorded and remain relatively constant during sunlight hours. At the same
838 time, intermediate Ångström ($0.7 - 1$) and FMF (~ 0.5) values, exhibiting weak temporal variation,
839 indicate a mixing state of fine and coarse aerosols.

Deleted: 4

Deleted: 2

Deleted: 1

Deleted: 1

Deleted: 13

Deleted: values

Formatted: Indent: First line: 1.27 cm

840 Aeolus backscatter retrievals at the regular (i.e., SCA; brown curve; Fig. 3-iv) and the mid-
841 bin (i.e., SCA mid-bin; black curve; Fig. 3-iv) vertical scales suffer from noise and retrieval gaps. As
842 a result, Aeolus detects incorrectly an aerosol layer between 5.5 and 8 km under the assumption that
843 clear-sky conditions are appropriately represented in the MSG-SEVIRI imagery and remain constant

863 within the time interval (~6 minutes) of MSG and Aeolus observations. At lower altitudes (2.5 – 4
864 km), due to the suspension of depolarizing mineral particles, a departure is marked between the pink
865 (linear-derived) and blue (Aeolus-like) Polly^{XT} profiles. Both SCA and SCA mid-bin fail to reproduce
866 the backscatter levels of this aerosol layer captured from the ground. In the lowest troposphere (<
867 2km), Aeolus overestimates significantly the backscatter coefficient but reproduces satisfactorily the
868 aerosol layer structure at the mid-bin vertical scale (i.e., SCA mid-bin; black curve; Fig. 3-iv), in
869 contrast to the regular scale (i.e., SCA; brown curve; Fig. 3-iv).

Formatted: Font: Not Bold

Deleted:

870 A general remark that should be made, is that for the cases analyzed, between the ground-
871 based and spaceborne profiles there is an inconsistency in the vertical representativeness within the
872 lowermost Aeolus bin. Under the absence of the near-field receivers (not considered in our study)
873 Polly^{XT} profiles are reported above ~800 m where the overlap between the laser beam and the receiver
874 telescope field of view is expected to be full. However, the base altitude of the near-surface Aeolus
875 bin is at ~200 m. This can interpret, at some degree, the large positive ALADIN-Polly^{XT} departures
876 at altitudes below 1 km, which are possibly further strengthened by an inappropriate RBS (i.e., low
877 SNR) in the Aeolus retrievals.

Deleted: It is reminded that SCA backscatter is actually retrieved whereas the SCA mid-bin results by averaging two consecutive bins following the procedure applied on the extinction for mitigating the downwards error propagation in the retrieval algorithm solution (Flament et al., 2021). At higher altitudes (2.5 – 4 km), due to the suspension of depolarizing mineral particles, a declination is marked between the pink (linear-derived) and blue (Aeolus-like) Polly^{XT} profiles. Again, the SCA mid-bin backscatter performs better than those of SCA reproducing more realistically the shape and the magnitude of the Polly^{XT} Aeolus-like profile. Finally, ALADIN detects aerosol layers between 5.5 and 8 km, assuming that clear-sky conditions are appropriately represented in the MSG-SEVIRI imagery and remain constant within the time interval (~6 minutes) of MSG and Aeolus observations, and the SCA mid-bin backscatter resides closer to the Polly^{XT} levels, which, however, are noisy.

878 879 6.2 Overall assessment and dependencies

880 In the second part of the analysis, an overall assessment of the Aeolus L2A retrievals is
881 performed by processing all the identified cases (43 in total; see Section 5). Due to the very limited
882 availability of ground-based extinction profiles, only the Aeolus L2A backscatter observations are
883 evaluated. It must be clarified that the evaluation of the Aeolus satellite (SAT) backscatter coefficient
884 is conducted without any conversion (i.e., from total linear to circular co-polar) of the ground-based
885 lidar (GRD) profiles. This has been decided since many of the SAT-GRD collocated samples are
886 derived from the Thessaloniki station. Due to technical issues (related to the polarization purity of the
887 emitted laser beam and the performance of the telescope lenses) no calibrated depolarizing
888 measurements, necessary to derive the Aeolus-like products (Paschou et al., 2021), are available for
889 the study period. Nevertheless, we are not expecting that this consideration, acknowledging that it is
890 imperfect, will affect substantially the robustness of our findings since in most of the study cases the
891 contribution of depolarizing particles is quite low based on the ancillary datasets/products. It is also
892 clarified that the Aeolus QA flags are not taken into account in the current study, since their validity
893 is not yet reliable (Reitebuch et al., 2020) as it has been demonstrated in Abril-Gago et al. (2022).
894 The discussion in the current section is divided in two parts. First, the vertically resolved evaluation
895 metrics are presented separately for the two Aeolus vertical scales, both for the unfiltered and the
896 filtered (cloud-free) profiles (Section 6.2.1). The same analysis format (i.e., SCA vs SCA mid-bin,

Moved (insertion) [2]

Deleted: ¶

917 unfiltered vs filtered) is kept in the second sub-section (Section 6.2.2) where the evaluation results
918 are presented as a function of various dependencies.

919

920 *6.2.1 Vertically resolved evaluation metrics*

921 In Figure 4, the vertically resolved bias (SAT-GRD; upper panel) and root mean square error
922 (RMSE; bottom panel) metrics are depicted for the unfiltered (cloud and aerosol backscatter) Aeolus
923 L2A backscatter retrievals, reported at the regular (left column) and the mid-bin (right column)
924 vertical scales. Bias and RMSE metrics [\(Wilks, 2019\)](#) are used in a complementary way in order to
925 avoid any misleading interpretation of the former score attributed to counterbalancing negative and
926 positive SAT-GRD deviations. For the calculation of the evaluation scores, the GRD profiles have
927 been rescaled to match Aeolus vertical product resolution. [To realize, we are calculating the averaged](#)
928 [values of the ground-based retrievals residing within the altitude margins of each Aeolus BRC.](#) Note
929 that in the SAT-GRD pairs, all BRCs from all cases are included (right y-axis in Figure 4), satisfying
930 the defined collocation criteria (see Section 5), and they are treated individually. [It is reminded that](#)
931 Aeolus L2A data are provided vertically at a constant number of range bins (i.e., 24 for SCA and 23
932 for SCA mid-bin) but their base altitude and their [thickness](#) vary along the orbit and from orbit-to-
933 orbit and they are defined dynamically (depending on the optimum SNR). Therefore, since the GRD
934 and SAT profiles are not interpolated in a common predefined grid, we are using as reference the
935 reverse index (with respect to those considered in the SCA retrieval algorithm in which 1 corresponds
936 to the top-most bin) of Aeolus SCA (from 1 to 24; left y-axis in Figs 4 i-a and ii-a) and SCA mid-bin
937 (from 1 to 23; left y-axis in Figs 4 i-b and ii-b) vertical scales.

Deleted: range

938 According to our results for the unfiltered Aeolus backscatter profiles (Fig. 4), positive biases
939 (up to $3.5 \text{ Mm}^{-1} \text{ sr}^{-1}$; red bars) are evident, at both vertical scales, at the first three bins (below 2 km).
940 For altitude ranges spanning from 2 to 8 km (bins 4 – 12), mainly positive SAT-GRD biases (up to
941 $\sim 1.5 \text{ Mm}^{-1} \text{ sr}^{-1}$) are recorded for SCA mid-bin whereas for SCA reach up to $\sim 1 \text{ Mm}^{-1} \text{ sr}^{-1}$ in absolute
942 terms. Similar tendencies are evident at the highest altitudes ($> 8 \text{ km}$) but the magnitude of the SAT-
943 GRD offsets becomes lower ($< 0.5 \text{ Mm}^{-1} \text{ sr}^{-1}$). Between the two Aeolus vertical scales, SCA mid-bin
944 performs better than SCA up to $\sim 8 \text{ km}$ (bin 12) and similar aloft, as it is shown by the RMSE profiles
945 (bottom panel in Fig. 4). Nevertheless, the most important finding is that Aeolus is not capable to
946 reproduce satisfactorily the backscatter profiles as it is revealed by the RMSE levels, which are
947 maximized near the ground ($\sim 8 \text{ Mm}^{-1} \text{ sr}^{-1}$), are considerably high (up to $6 \text{ Mm}^{-1} \text{ sr}^{-1}$) in the free
948 troposphere and are minimized ($< 1 \text{ Mm}^{-1} \text{ sr}^{-1}$) at the uppermost bins. Our findings are highly
949 consistent with those presented in Abril-Gago et al. (2022), who performed a validation of Aeolus
950 L2A particle backscatter coefficient against reference measurements obtained at three

Deleted: 5

953 ACTRIS/EARLINET sites in the Iberian Peninsula. Several factors contribute to the obtained height-
954 dependent SAT-GRD discrepancies. Near the ground, the observed maximum overestimations are
955 mainly attributed to the: (i) contamination of the ALADIN lidar signal by surface reflectance, (ii)
956 increased noise in the lowermost bins (caused by the non-linear approach retrieving the backscatter
957 coefficient) as it has been pointed out also in the atmospheric simulations cases I and II in Ehlers et
958 al. (2022) and (iii) limited vertical representativeness of the GRD profiles below 1 km. On the
959 contrary, in the free troposphere, the cloud contamination on spaceborne retrievals plays a dominant
960 role on the occurrence of ALADIN backscatter overestimations with respect to the cloud-free ground-
961 based retrievals. From a statistical point of view, it must also be mentioned that the robustness of the
962 bias and RMSE metrics decreases for the increasing altitudes due to the reduction of the number of
963 the SAT-GRD matchups (right y-axis in Fig. 4) participating in the calculations.

964 The assessment analysis has been repeated after removing Aeolus profiles when clouds are
965 detected by MSG-SEVIRI (grey shaded areas in Fig. 1) within a BRC (colored rectangles in Fig. 1).
966 By contrasting Figures 4 and 5 (evaluation metrics for the filtered profiles), an expected improvement
967 of the level of agreement between SAT and GRD is visible. This translates into a drastic reduction of
968 bias and RMSE levels at altitude ranges up to 5-6 km (~bin 10). Between bins 2 and 5 slight
969 underestimations (blue bars) and overestimations (red bars) are found for SCA (Fig. 5 i-a). On the
970 contrary, for the SCA mid-bin (Fig. 5 i-b), low positive SAT-GRD offsets are recorded, due to the
971 omitted negative backscatter values, as it will be shown in the next section. Above bin 5, SAT-GRD
972 deviations are low in absolute terms, oscillating around zero, for SCA, whereas only positive SAT-
973 GRD biases are recorded for SCA mid-bin, which are maximized ($\sim 0.7 \text{ Mm}^{-1} \text{ sr}^{-1}$) at the highest bins
974 and are associated with limited SAT-GRD matchups (right x-axis in Fig. 5 i-b). The obtained
975 improvements on bias scores become more confident since they are associated with similar strong
976 reductive tendencies on RMSE levels. More specifically, the RMSE spikes of extremely high values
977 recorded in the unfiltered profiles either disappear or weaken in the case of the Aeolus filtered SCA
978 (Fig. 5 ii-a) and SCA mid-bin (Fig. 5 ii-b) backscatter profiles. However, even though the RMSE
979 values at the lowermost bins (close to the ground) are decreased when cloud contaminated Aeolus
980 profiles are eliminated, still the corresponding levels for the filtered profiles are considerably high
981 attributed to the lower SNR and the possible impact of surface returns.

983 6.2.2 Scatterplots

984 An alternative approach to assess the performance of Aeolus L2A backscatter is attempted
985 here by reproducing two dimensional histograms for the entire SAT-GRD collocated sample as well
986 as scatterplots resolved based on various dependencies, aiming to investigate the factors determining

Deleted: dependen

Deleted: values

Deleted: 2

Deleted: whereas

Formatted: English (United States)

Deleted: for SCA mid-bin (Fig. 5 i-b)

Formatted: Font: (Default) Times New Roman, 12 pt

Formatted: Font: (Default) Times New Roman, 12 pt, Not Bold

Formatted: Font: (Default) Times New Roman, 12 pt

Deleted:)

Formatted: Font: (Default) Times New Roman, 12 pt, Not Bold

Deleted: higher

995 the level of agreement between spaceborne and ground-based retrievals. More specifically, the
996 dependencies under investigation are those of the: (i) station locations, (ii) BRCs and (iii) orbits (dawn
997 vs dusk). The evaluation metrics have been calculated for all possible combinations of vertical scales
998 (SCA vs SCA mid-bin) and Aeolus profiles (unfiltered vs filtered).

999 Figure 6 depicts the two-dimensional histograms between GRD (x-axis) and SAT (y-axis)
1000 backscatter coefficient for the raw (upper panel) and filtered (bottom panel) Aeolus profiles reported
1001 at the SCA (left column) and SCA mid-bin (right column) vertical scales. Note that we have removed
1002 SAT-GRD pairs in which Aeolus backscatter exceeds $20 \text{ Mm}^{-1} \text{ sr}^{-1}$ in order to avoid the
1003 “contamination” of extreme outliers in the calculated metrics, possibly attributed to the presence of
1004 clouds (Proestakis et al., 2019).

1005 Between the SCA and SCA mid-bin unfiltered retrievals, it is found that the correlation
1006 coefficients (0.36 and 0.39, respectively) and RMSEs (2.00 and 1.88, respectively) are similar
1007 whereas there is an evident difference on the biases (0.45 $\text{Mm}^{-1} \text{ sr}^{-1}$ and 0.69 $\text{Mm}^{-1} \text{ sr}^{-1}$, respectively).
1008 Nevertheless, it is noted that less SAT-GRD pairs are recorded for SCA mid-bin due to the inherent
1009 flagging of negative values. After removing cloud-contaminated Aeolus profiles, the amount of the
1010 SAT-GRD matchups is reduced by about 55% and 59% for SCA (from 537 to 239) and SCA mid-
1011 bin (from 356 to 147), respectively. Nevertheless, thanks to this filtering procedure, the initially
1012 observed overestimations for SCA and SCA mid-bin are reduced by ~25% and ~43%, respectively,
1013 whereas the RMSE values drop down to 1.65 (SCA) and 1.00 (SCA mid-bin). The better agreement
1014 between SAT and GRD, for the filtered Aeolus profiles, is further justified by the increase of the R
1015 values (from 0.39 to 0.48) for the SCA mid-bin whereas for SCA there is no positive or negative
1016 tendency ($R=0.36$). The spread of the points in the two dimensional space reveals many similarities
1017 with the corresponding scatterplots presented in Abril-Gago et al. (2022) for the Iberian
1018 ACTRIS/EARLINET stations.

1019 A common feature in all scatterplots, shown in Figure 6, is that most of the positive outliers
1020 are found at the lowermost bins (see Figs. 4 and 5). SAT beta can reach up to $20 \text{ Mm}^{-1} \text{ sr}^{-1}$ in contrast
1021 to the corresponding GRD levels, which are mainly lower than $2 \text{ Mm}^{-1} \text{ sr}^{-1}$. For SCA (Figs. 6 i-a, 6
1022 ii-a), the majority of the negative SAT-GRD pairs are recorded at the highest bins in which, however,
1023 both spaceborne and ground-based backscatter coefficients are noisy. Another cluster of SAT-GRD
1024 pairs is those where slight negative Aeolus backscatter values are grouped together with low positive
1025 backscatter values retrieved from ground. At the mid-bin vertical scale, for the unfiltered Aeolus
1026 profiles (Fig. 6 i-b), the negative SAT backscatter values are masked out resulting in better evaluation
1027 metrics (except the increase of bias due to the removal of the negative Aeolus backscatter) with
1028 respect to the regular vertical scale. Among the four scatterplots, the best agreement between Aeolus

Moved up [2]: It is also clarified that the Aeolus QA flags are not taken into account in the current study, since their validity is not yet reliable (Reitebuch et al., 2020) as it has been demonstrated in Abril-Gago et al. (2022).

Deleted: there is a contradiction of which performs better relying on the correlation coefficient (0.36 and 0.39, respectively).

Formatted: Font: (Default) Times New Roman, 12 pt, Not Bold

Formatted: Font: (Default) Times New Roman, 12 pt, Not Bold

Formatted: Font: (Default) Times New Roman, 12 pt, Not Bold

Formatted: Font: (Default) Times New Roman, 12 pt, Not Bold

Deleted: and RMSE (2.00 and 1.88, respectively) metrics.

Deleted: t any

1038 and ground-based retrievals is revealed for the SCA mid-bin filtered profiles (Fig. 6 ii-b) attributed
1039 to the coincident elimination of the negative and the extreme positive Aeolus backscatter coefficient.

1040 Figure 7 depicts the overall scatterplot between ground-based and spaceborne retrievals as a
1041 function of the three PANACEA sites (colored categories). The associated evaluation scores are
1042 summarized in Table 1 and 2 for the unfiltered and filtered Aeolus profiles, respectively. The majority
1043 of the extreme positive outliers of unfiltered SCA retrievals (Fig. 7 i-a) are recorded in Thessaloniki
1044 and Athens. According to our results, significant biases ($0.73 \text{ Mm}^{-1} \text{ sr}^{-1}$ for ATH and $0.83 \text{ Mm}^{-1} \text{ sr}^{-1}$
1045 for THE) and high RMSE values ($2.26 \text{ Mm}^{-1} \text{ sr}^{-1}$ for ATH and $2.60 \text{ Mm}^{-1} \text{ sr}^{-1}$ for THE) are found. At
1046 Antikythera island (ANT), the biases are quite low and equal to $0.06 \text{ Mm}^{-1} \text{ sr}^{-1}$ and 13.6% in absolute
1047 and relative terms, respectively (Table 1). In all stations, for the unfiltered SCA mid-bin retrievals,
1048 the absolute SAT-GRD departures become larger whereas the RMSE decreases in ANT/THE and
1049 increases in ATH. Regarding the temporal covariation between SAT and GRD retrievals, a noticeable
1050 improvement is evident in ANT (i.e., R increases from 0.49 to 0.57). For the quality-assured Aeolus
1051 profiles (Table 2), all evaluation metrics converge towards the ideal scores for SCA mid-bin whereas
1052 mainly positive tendencies (i.e., better agreement) are evident for SCA. Overall, among the three
1053 stations the best performance of Aeolus is recorded at the Antikythera island.

1054 Between dawn (descending) and dusk (ascending) orbits, better bias and RMSE scores are
1055 computed when Aeolus is flying during early morning hours while better R values are found during
1056 early afternoon satellite overpasses. However, our orbit-wise results are not robust since the number
1057 of Aeolus overpasses is not evenly distributed (about 85% of the SAT-GRD matchups are acquired
1058 during dawn orbits). Among the three BRCs (red, blue or magenta), which can satisfy the defined
1059 SAT-GRD spatial criterion (see Section 5) the best metrics are found for the red BRC residing most
1060 of the cases closer to the station site.

1062 7. Discussion on Cal/Val aspects and recommendations

1063

1064 Throughout this assessment analysis, several critical points have been identified and
1065 highlighted that should be addressed adequately towards a comprehensive Cal/Val study of the
1066 Aeolus L2A products. These aspects can: (i) serve as guidelines for future relevant studies, (ii)
1067 improve our understanding about the advantages/limitations of Aeolus data in terms of their
1068 usefulness and applicability in aerosol-related studies and (iii) suggest possible upgrades regarding
1069 ALADIN's observational capabilities, the considerations of the applied retrieval algorithms and the
1070 content of information in Aeolus L2A data.

Deleted: overestimations

Deleted: based

Deleted: aerosol

Deleted: , summarized in the current section,

1075 A fair comparison of Aeolus L2A backscatter versus linear-derived retrievals acquired from
1076 ground-based lidars, when depolarizing particles are recorded, requires the conversion of the latter
1077 ones to circular co-polar (Aeolus-like) following Paschou et al. (2021). Nevertheless, it should be
1078 acknowledged that the theoretical assumptions can be invalid either due to the orientation of the
1079 suspended particles (e.g., mineral dust; Ulanowski et al., 2007; Daskalopoulou et al., 2021; Mallios
1080 et al., 2021) or due to multiple scattering effects within optically thick aerosol layers (Wandinger et
1081 al., 2010). The lack of aerosols/clouds discrimination in Aeolus L2A data forces the synergistic
1082 implementation of ancillary data in order to remove cloud contaminated Aeolus profiles from the
1083 collocated sample with the cloud-free ground-based profiles. Nevertheless, it should be noted that the
1084 cloud removal itself is not perfect. In our case, we are relying on MSG-SEVIRI cloud observations,
1085 which are available at high temporal frequency (every 15 min) thus allowing a very good temporal
1086 collocation with Aeolus. The indirect cloud-mask filtering applied to our analysis, leads to a
1087 substantial improvement of the level of agreement between spaceborne and ground-based retrievals.
1088 Despite its success, our proposed approach provides a sufficient and acceptable solution, but
1089 undoubtedly cannot be superior to the utility of a descriptive classification scheme on Aeolus retrieval
1090 algorithms similarly done in CALIOP-CALIPSO (Liu et al., 2019; Zeng et al., 2019).

1091 Aeolus retrievals are available at coarse along-track resolution (~90 km). This imposes
1092 limitations on their evaluation against point measurements, which are further exacerbated at sites
1093 where the heterogeneity of aerosol loads in the surrounding area of the station is pronounced, taking
1094 into account that the spatial collocation between spaceborne and ground-based retrievals is not exact.
1095 Numerical outputs from reanalysis datasets (e.g., MERRA-2, CAMS) can be utilized as an indicator
1096 of aerosols' burden horizontal variation, taking advantage of their complete spatial coverage, their
1097 availability at high temporal frequency and their reliability in terms of total AOD (Innes et al., 2019;
1098 Gueymard and Yang, 2020). Nevertheless, such data are better to be utilized in a qualitative rather
1099 than a quantitative way, particularly in terms of aerosol species, since they cannot be superior of
1100 actual aerosol observations. Over areas with a complex terrain, vertical inconsistencies between
1101 ground-based and satellite profiles (reported above ground where its height is defined with respect to
1102 the WGS 84 ellipsoid), not physically explained. can be recorded. For the derivation of the evaluation
1103 scores, it is required a rescaling of the ground-based profiles, acquired at finer vertical resolution, in
1104 order to match the dynamically defined Aeolus' range bin settings. Nevertheless, due to this
1105 transformation, the shape of the raw ground-based profile can be distorted and the magnitude of the
1106 retrieved optical properties can be modified substantially thus affecting the evaluation metrics. This
1107 artifact is evident in cases where the vertical structure of the aerosol layers is highly variable thus
1108 hindering Aeolus capability to reproduce accurately their geometrical features. Finally, the

Deleted: between aerosols and clouds

Deleted:

Deleted: due to the coarse BRC horizontal resolution, they
can be recorded

Deleted: due to the coarse vertical resolution in which
optical products are derived

1115 consideration of backward trajectories can assist the characterization of the probed atmospheric scene
1116 by Aeolus. Potentially, they can be also used as an additional criterion for the optimum selection of
1117 Aeolus BRC for the collocation with the ground-based measurements. However, possible limitations
1118 may arise due to temporal deviations among FLEXPART run, the Aeolus overpass and ground-based
1119 retrievals, which might be critical taking into account the strong spatiotemporal variability of aerosol
1120 loads across various scales.

1121

1122 8. Conclusions

1123 The limited availability of vertically resolved aerosol products from space constitutes a major
1124 deficiency of the Global Observing System (GOS). The launch of the Aeolus ESA satellite was a
1125 major step towards this direction whereas the forthcoming EarthCARE satellite mission (Illingworth
1126 et al., 2015) will accelerate further these efforts. ALADIN, the single payload of the Aeolus satellite,
1127 constitutes the first UV HSRL Doppler lidar ever placed in space and it is optimized to acquire HLOS
1128 wind profiles towards advancing numerical weather prediction (Rennie et al., 2021). ALADIN also
1129 retrieves independently the extinction and backscatter coefficients of aerosols and clouds (grouped as
1130 particulates according to Aeolus' nomenclature) via the implementation of the SCA algorithm.

1131 The current work focuses on the assessment of the SCA backscatter coefficients versus
1132 ground-based retrievals acquired routinely by lidar systems operating in Athens, Thessaloniki, and
1133 Antikythera. The aforementioned stations contribute to the PANACEA Greek National Research
1134 Infrastructure (Greek ACTRIS component) and to the European Aerosol Research Lidar Network
1135 (EARLINET; Pappalardo et al., 2014). Overall, 43 cases are analyzed out of which 12 have been
1136 identified in the urban site of Athens, 16 in Thessaloniki and 15 in the remote site of the Antikythera
1137 island.

1138 In the first part of the analysis, focus was given on the assessment of Aeolus L2A particle
1139 backscatter coefficient, under specific aerosol scenarios, versus the corresponding measurements
1140 obtained at the Antikythera island (southwest Greece). As expected, the misdetection of the cross
1141 polarized lidar return signals, induces an underestimation (ranging from 13% to 33%) of Aeolus L2A
1142 backscatter when depolarizing mineral particles are probed (case of 10th July 2019). For the case of
1143 3rd July 2019, when aerosol loads of moderate intensity, consisting mainly of spherical particles, are
1144 confined below 4 km and they are homogeneous in the surrounding area of the station, Aeolus' SCA
1145 backscatter product is capable in reproducing quite well the ground-based profile in terms of shape
1146 and magnitude. For the cases of 8th July 2020 and 5th August 2020, Aeolus performance in terms of
1147 depicting complex stratified aerosol layers (composed of particles of different origin), as these are

Deleted: ¶

Deleted: analysis

Deleted: L2A particle

Deleted: 6

Deleted: .

Deleted: By converting the ground-based linear-derived total backscatter to circular co-polar (i.e., Aeolus-like) it is computed that these underestimations range from 13% to 33%

Formatted: English (United States)

Formatted: Superscript

Formatted: Superscript

1157 observed from ground, downgrades due to noise in the cross-talk corrected molecular and particulate
1158 signals.

1159 From our statistical assessment analysis, it has been revealed that the removal of cloud
1160 contaminated spaceborne profiles, achieved via the synergy with MSG-SEVIRI cloud observations,
1161 results in a significant improvement of the product performance. Unfortunately, the poor evaluation
1162 metrics at the lowermost bins (attributed to either the surface reflectance or the increased noise levels
1163 for the Aeolus retrievals and to the overlap issues for the ground-based profiles) are still evident after
1164 the cloud filtering procedure. Between the two Aeolus vertical scales, the computed evaluation
1165 metrics do not provide strong evidence of which of them performs better. Among the three stations
1166 (ATH, ANT, THE) considered here, the best agreement was found in the remote site of Antikythera
1167 island in contrast to the urban sites of Athens and Thessaloniki. All key Cal/Val aspects, serving as
1168 guidelines and potential recommendations for future studies, have been discussed thoroughly.

1169 In the current work, we emphasized only on the particle backscatter coefficient due to the
1170 limited number of ground-based extinction profiles. A wider assessment analysis is ongoing in the
1171 framework of the Aeolus L2A Cal/Val study performed within EARLINET. Finally, the best
1172 assessment of Aeolus L2A products is expected versus the purpose-built eVe lidar (Paschou et al.,
1173 2021). Thanks to its configuration, eVe can mimic Aeolus' observational geometry and test the
1174 validity of the theoretical formulas applied for the derivation of the Aeolus-like backscatter from the
1175 linearly polarized emission ground-based systems. The first correlative Aeolus-eVe measurements
1176 have been performed in the framework of the Joint Aeolus Tropical Atlantic Campaign (JATAC),
1177 that took place in Cape Verde in September 2021. Correlative measurements are also acquired during
1178 the ESA-ASKOS experimental campaign (Mindelo, Cabo Verde). The geographical location of Cabo
1179 Verde, situated on the "corridor" of the Saharan transatlantic transport (Gkikas et al., 2022), is ideal
1180 for assessing Aeolus performance when non-spherical mineral particles from the nearby deserts are
1181 adverted westwards.

1182 1183 Acknowledgments

1184 Antonis Gkikas was supported by the Hellenic Foundation for Research and Innovation (H.F.R.I.)
1185 under the "2nd Call for H.F.R.I. Research Projects to support Post-Doctoral Researchers" (project
1186 acronym: ATLANTAS, project number: 544). Vassilis Amiridis acknowledges support from the
1187 European Research Council (grant no. 725698; D-TECT). NOA members acknowledge support from
1188 the Stavros Niarchos Foundation (SNF). We acknowledge support of this work by the project
1189 "PANhellenic infrastructure for Atmospheric Composition and climatE change" (MIS 5021516)
1190 which is implemented under the Action "Reinforcement of the Research and Innovation

Deleted: On the contrary, in the case of 8th July 2020, when the stratification of aerosol layers, detected up to 4 km by Polly^{XT}, becomes complex, Aeolus' performance reveals an altitude dependency, probably attributed to the coarse vertical sampling of the atmosphere. Finally, the agreement between Aeolus and Polly^{XT} backscatter retrievals varies with height on 5th August 2020 when non-spherical particles (2-4 km) reside on top of a layer consisting of spherical aerosols.

Deleted: (spatially homogeneous AODs) i

Deleted: c

Deleted: v

Deleted: serving as guidelines and potential recommendations for future studies

Deleted: The lack of the cross-polar channel downgrades ALADIN's performance under depolarizing atmospheric scenes (e.g., dust, cirrus crystals, volcanic ash) hampering an effective aerosols/clouds discrimination (Flamant et al., 2021). According to preliminary CAMS assimilation experiments (A3S), relying on Aeolus L2A backscatter, it has been demonstrated to have a beneficial impact on short-term forecasts. However, it is under investigation if the inclusion of the cross-polar channel will expand these positive feedbacks on NWP (main scientific goal of the Aeolus satellite mission), taking into account that aerosol-radiation interactions affect atmospheric dynamics and vice-versa. Another important aspect is the coarse resolution of Aeolus L2A retrievals, both in horizontal and vertical, imposing several limitations in an appropriate assessment analysis whereas it can be critical in their implementation on other applications (e.g. data assimilation). ¶

Deleted: study

Deleted: Taking into account the challenges that the SCA algorithm faces in retrieving the extinction coefficient reliably (Flamant et al., 2021), new retrievals will become available in the Aeolus L2A product. These include the Maximum Likelihood Estimate (MLE) (Ehlers et al., 2021) and the EarthCARE derived AEOL-FF and AEL-PRO products (refer to the latest L2A product release documentation).

Deleted: implemented in a dual-laser/dual-telescope configuration enabling the simultaneous emission of linearly and circularly polarized radiation at 355 nm and the detection of the elastically backscattered radiation with polarization sensitive channels as well as the inelastic (Raman) backscattered radiation at 387 nm

Deleted: As such,

Deleted: planned

Deleted: in June 2022 at the same place

Deleted: pe

Deleted: ¶

Deleted:

Formatted: Superscript

1242 Infrastructure", funded by the Operational Programme "Competitiveness, Entrepreneurship and
1243 Innovation" (NSRF 2014-2020) and co-financed by Greece and the European Union (European
1244 Regional Development Fund). We thank the ACTRIS-2 and ACTRIS preparatory phase projects that
1245 have received funding from the European Union's Horizon 2020 Framework Program for Research
1246 and Innovation (grant agreement no. 654109) and from European Union's Horizon 2020 Coordination
1247 and Support Action (grant agreement no. 739530), respectively. This research was also supported by
1248 data and services obtained from the PANhellenic Geophysical Observatory of Antikythera
1249 (PANGEA) of the National Observatory of Athens (NOA). We acknowledge support by ESA, in the
1250 framework of the Aeolus+Innovation (Aeolus+I) call, under Contract No. 4000133130/20/I-BG//.
1251

1252 **Data availability**

1253 Aeolus Baseline ~~11~~ L2A data were obtained from the ESA Aeolus Online Dissemination System
1254 available at <https://aeolus-ds.eo.esa.int/oads/access/>.

Deleted: 10 and

1255

1256 **References**

1257 Abril-Gago, J., Guerrero-Rascado, J. L., Costa, M. J., Bravo-Aranda, J. A., Sicard, M., Bermejo-
1258 Pantaleón, D., Bortoli, D., Granados-Muñoz, M. J., Rodríguez-Gómez, A., Muñoz-Porcar, C.,
1259 Comerón, A., Ortiz-Amezcu, P., Salgueiro, V., Jiménez-Martín, M. M., and Alados-Arboledas, L.:
1260 Statistical validation of Aeolus L2A particle backscatter coefficient retrievals over
1261 ACTRIS/EARLINET stations on the Iberian Peninsula, *Atmos. Chem. Phys.*, 22, 1425–1451,
1262 <https://doi.org/10.5194/acp-22-1425-2022>, 2022.

1263

1264 Amiridis, V., Balis, D. S., Giannakaki, E., Stohl, A., Kazadzis, S., Koukouli, M. E., and Zanis, P.:
1265 Optical characteristics of biomass burning aerosols over Southeastern Europe determined from UV-
1266 Raman lidar measurements, *Atmos. Chem. Phys.*, 9, 2431–2440, <https://doi.org/10.5194/acp-9-2431-2009>, 2009.

1268

1269 Amiridis, V., Giannakaki, E., Balis, D. S., Gerasopoulos, E., Pytharoulis, I., Zanis, P., Kazadzis, S.,
1270 Melas, D., and Zerefos, C.: Smoke injection heights from agricultural burning in Eastern Europe as
1271 seen by CALIPSO, *Atmos. Chem. Phys.*, 10, 11567–11576, <https://doi.org/10.5194/acp-10-11567-2010>, 2010.

1273

1275 Amiridis, V., Zerefos, C., Kazadzis, S., Gerasopoulos, E., Eleftheratos, K., Vrekoussis, M., Stohl, A.,
1276 Mamouri, R.E., Kokkalis, P., Papayannis, A., et al.: Impact of the 2009 Attica wildfires on the air
1277 quality in urban Athens, *Atmos. Environ.*, 46, 536–544,
1278 <https://doi.org/10.1016/j.atmosenv.2011.07.056>, 2012.

1279

1280 Amodeo, Aldo, D'Amico, Giuseppe, Giunta, Aldo, Papagiannopoulos, Nikolaos, Papayannis, Alex,
1281 Argyrouli, Athina, Mylonaki, Maria, Tsaknakis, Georgios, Kokkalis, Panos, Soupiona, Ourania,
1282 Tzanis, Chris. (2018). ATHLI16: the ATHens Lidar Intercomparison campaign. *EPJ Web of*
1283 *Conferences*. 176. 09008. 10.1051/epjconf/201817609008.

1284

1285 [Anderson, T. L., Charlson, R. J., Winker, D. M., Ogren, J. A., and Holmén, K.: Mesoscale Variations](https://doi.org/10.1175/1520-0469(2003)060<0119:MVOTA>2.0.CO;2)
1286 [of Tropospheric Aerosols, *J. Atmos. Sci.*, 60, 119–136, https://doi.org/10.1175/1520-](https://doi.org/10.1175/1520-0469(2003)060<0119:MVOTA>2.0.CO;2)
1287 [0469\(2003\)060<0119:MVOTA>2.0.CO;2, 2003.](https://doi.org/10.1175/1520-0469(2003)060<0119:MVOTA>2.0.CO;2)

1288

1289 Ansmann, A., Petzold, A., Kandler, K., Tegen, I., Wendisch, M., Müller, D., Weinzierl, B., Müller,
1290 T. and Heintzenberg, J.: Saharan Mineral Dust Experiments SAMUM–1 and SAMUM–2: what have
1291 we learned?, *Tellus B: Chemical and Physical Meteorology*, 63(4), 403–429, doi:10.1111/j.1600-
1292 0889.2011.00555.x, 2011.

1293

1294 Ansmann, A., Wandinger, U., Riebesell, M., Weitkamp, C., Michaelis, W.: Independent measurement
1295 of extinction and backscatter profiles in cirrus clouds by using a combined raman elastic-backscatter
1296 lidar, *Applied Optics*, 31, 7113-7131, doi: 10.1364/AO.31.007113, 1992.

1297

1298 Baars, H., et al. : An overview of the first decade of PollyNET: an emerging network of automated
1299 Raman-polarization lidars for continuous aerosol profiling, *Atmos. Chem. Phys.*, 16, 5111–5137,
1300 <https://doi.org/10.5194/acp-16-5111-2016>, 2016.

1301

1302 Baars, H., Ansmann, A., Ohneiser, K., Haarig, M., Engelmann, R., Althausen, D., Hanssen, I., Gausa,
1303 M., Pietruczuk, A., Szkop, A., Stachlewska, I. S., Wang, D., Reichardt, J., Skupin, A., Mattis, I.,
1304 Trickl, T., Vogelmann, H., Navas-Guzmán, F., Haefele, A., Acheson, K., Ruth, A. A., Tatarov, B.,
1305 Müller, D., Hu, Q., Podvin, T., Goloub, P., Veselovskii, I., Pietras, C., Haefelin, M., Fréville, P.,
1306 Sicard, M., Comerón, A., Fernández García, A. J., Molero Menéndez, F., Córdoba-Jabonero, C.,
1307 Guerrero-Rascado, J. L., Alados-Arboledas, L., Bortoli, D., Costa, M. J., Dionisi, D., Liberti, G. L.,
1308 Wang, X., Sannino, A., Papagiannopoulos, N., Boselli, A., Mona, L., D'Amico, G., Romano, S.,

- 1309 Perrone, M. R., Belegante, L., Nicolae, D., Grigorov, I., Gialitaki, A., Amiridis, V., Soupiona, O.,
1310 Papayannis, A., Mamouri, R.-E., Nisantzi, A., Heese, B., Hofer, J., Schechner, Y. Y., Wandinger, U.,
1311 and Pappalardo, G.: The unprecedented 2017–2018 stratospheric smoke event: decay phase and
1312 aerosol properties observed with the EARLINET, *Atmos. Chem. Phys.*, 19, 15183–15198,
1313 <https://doi.org/10.5194/acp-19-15183-2019>, 2019.
- 1314
- 1315 Baars, H., Herzog, A., Heese, B., Ohneiser, K., Hanbuch, K., Hofer, J., Yin, Z., Engelmann, R., and
1316 Wandinger, U.: Validation of Aeolus wind products above the Atlantic Ocean, *Atmos. Meas. Tech.*,
1317 13, 6007–6024, <https://doi.org/10.5194/amt-13-6007-2020>, 2020.
- 1318
- 1319 Baars, H., Radenz, M., Floutsi, A. A., Engelmann, R., Althausen, D., Heese, B., Ansmann, A.,
1320 Flament, T., Dabas, A., Trapon, D., Reitebuch, O., Bley, S., and Wandinger, U.: Californian wildfire
1321 smoke over Europe: A first example of the aerosol observing capabilities of Aeolus compared to
1322 ground-based lidar, *Geophys. Res. Lett.*, 48, e2020GL092194,
1323 <https://doi.org/10.1029/2020GL092194>, 2021.
- 1324
- 1325 Balis, D., Amiridis, V., Nickovic, S., Papayannis, A., and Zerefos, C.: Optical properties of Saharan
1326 dust layers as detected by a Raman lidar at Thesaloniki, Greece, *Geophys. Res. Lett.*, 31, L13104,
1327 <https://doi.org/10.1029/2004GL019881>, 2004
- 1328
- 1329 Balis, D., Amiridis, V., Kazadzis, S., Papayannis, A., Tsaknakis, G., Tzortzakis, S., Kalivitis, N.,
1330 Vrekoussis, M., Kanakidou, M., Mihalopoulos, N., Chourdakis, G., Nickovic, S., Pérez, C.,
1331 Baldasano, J., and Drakakis, M.: Optical characteristics of desert dust over the East Mediterranean
1332 during summer: a case study, *Ann. Geophys.*, 24, 807–821, <https://doi.org/10.5194/angeo-24-807-2006>, 2006.
- 1334
- 1335 Brioude, J., Arnold, D., Stohl, A., Cassiani, M., Morton, D., Seibert, P., Angevine, W., Evan, S.,
1336 Dingwell, A., Fast, J.D., Easter, R.C., Pisso, I., Burkhardt, J., Wotawa, G., 2013. The Lagrangian
1337 particle dispersion model FLEXPART-WRF version 3.1. *Geosci. Model. Dev.* 6, 1889e1904.
1338 <http://dx.doi.org/10.5194/gmd-6-1889-2013>.
- 1339
- 1340 Bohlmann, S., Baars, H., Radenz, M., Engelmann, R., and Macke, A.: Ship-borne aerosol profiling
1341 with lidar over the Atlantic Ocean: from pure marine conditions to complex dust–smoke mixtures,
1342 *Atmos. Chem. Phys.*, 18, 9661–9679, <https://doi.org/10.5194/acp-18-9661-2018>, 2018.

1343
1344 Boucher, O., Randall, D., Artaxo, P., Bretherton, C., Feingold, G., Forster, P., Kerminen, V.-M.,
1345 Kondo, Y., Liao, H., Lohmann, U., Rasch, P., Satheesh, S., Sherwood, S., Stevens, B., and Zhang,
1346 X.: Clouds and Aerosols, in: Climate Change 2013: The Physical Science Basis. Contribution of
1347 Working Group I to the Fifth Assessment Report of the Intergovernmental Panel on Climate Change,
1348 edited by Stocker, T., Qin, D., Plattner, G.-K., Tignor, M., Allen, S., Boschung, J., Nauels, A., Xia,
1349 Y., Bex, V., and Midgley, P., chap. 7, pp. 571–658, Cambridge University Press, Cambridge, United
1350 Kingdom and New York, NY, USA, <https://doi.org/10.1017/CBO9781107415324.016>, 2013.
1351
1352 Buchard, V., Randles, C. A., da Silva, A. M., Darmenov, A., Colarco, P. R., Govindaraju, R., Ferrare,
1353 R., Hair, J., Beyersdorf, A. J., Ziemba, L. D. and Yu, H.: The MERRA-2 aerosol reanalysis, 1980
1354 onward. Part II: Evaluation and case studies, *J. Climate*, 30, 6851–6872,
1355 <https://doi.org/10.1175/JCLI-D-16-0613.1>, 2017.
1356
1357 Campbell, J. R., Hlavka, D. L., Welton, E. J., Flynn, C. J., Turner, D. D., Spinhirne, J. D., Scott, V.
1358 S., and Hwang, I. H.: Full-time eye-safe cloud and aerosol lidar observation at Atmospheric Radiation
1359 Measurement program sites: Instruments and data processing, *J. Atmos. Oceanic Technol.*, 19, 431–
1360 442, 2002.
1361
1362 Charlson, R. J., Schwartz, S. E., Hales, J. M., Cess, R. D., Coakley, J. A., Hansen, J. E., and Hofmann,
1363 D. J.: Climate Forcing by Anthropogenic Aerosols, *Science*, 255, 423–430,
1364 <https://doi.org/10.1126/science.255.5043.423>, 1992.
1365
1366 Collis, R. and Russell, P.: Lidar measurement of particles and gases by elastic backscattering and
1367 differential absorption, chap. Lidar measurement of particles and gases by elastic backscattering and
1368 differential absorption, Springer, Berlin, Heidelberg, 71– 151, https://doi.org/10.1007/3-540-07743-X_18, 1976.
1370
1371 Dabas, A.: Generation of AUX_CAL: Detailed Processing Model and Input/Output Data Definition,
1372 software, ESA, available at: <https://earth.esa.int/eogateway/documents/20142/1564626/Aeolus-Calibration-Processor-Documentation.zip> (last access: 20 February 2022), 2017.
1374

1375 D'Amico, G., Amodeo, A., Mattis, I., Freudenthaler, V., and Pappalardo, G.: EARLINET Single
1376 Calculus Chain – technical – Part 1: Pre-processing of raw lidar data, *Atmos. Meas. Tech.*, 9, 491–
1377 507, <https://doi.org/10.5194/amt-9-491-2016>, 2016.

1378
1379 Daskalopoulou, V., Raptis, I. P., Tsekeli, A., Amiridis, V., Kazadzis, S., Ulanowski, Z., Metallinos,
1380 S., Tassis, K., and Martin, W.: Monitoring dust particle orientation with measurements of sunlight
1381 dichroic extinction, 15th International Conference on Meteorology, Climatology and Atmospheric
1382 Physics (COMECP 2021), Ioannina, Greece, 26–29 September 2021, Zenodo [conference paper],
1383 <https://doi.org/10.5281/zenodo.5075998>, 2021.

1384
1385 Derrien, M. and Le Gleau, H.: MSG/SEVIRI cloud mask and type from SAFNWC, *Int. J. Remote Sens.*, 26, 4707–4732, 2005.

1387
1388 [Dubovik, O., Holben, B. N., Eck, T. F., Smirnov, A., Kaufman, Y. J., King, M. D., Tanré, D., and Slutsker, I.: Variability of Absorption and Optical Properties of Key Aerosol Types Observed in Worldwide Locations, *J. Atmos. Sci.*, 59, 590–608, 2002.](#)

1391
1392 ECMWF: ECMWF starts assimilating Aeolus wind data, <https://www.ecmwf.int/en/about/media-centre/news/2020/ecmwf-starts-assimilating-aeolus-wind-data>, last access: 12 June 2020, 2020.

1394
1395 [Ehlers, F., Flament, T., Dabas, A., Trapon, D., Lacour, A., Baars, H., and Straume-Lindner, A. G.: Optimization of Aeolus' aerosol optical properties by maximum-likelihood estimation, *Atmos. Meas. Tech.*, 15, 185–203, <https://doi.org/10.5194/amt-15-185-2022>, 2022.](#)

1398
1399 Engelmann, R., Kanitz, T., Baars, H., Heese, B., Althausen, D., Skupin, A., Wandinger, U.,
1400 Komppula, M., Stachlewska, I. S., Amiridis, V., Marinou, E., Mattis, I., Linné, H., and Ansmann, A.:
1401 The automated multiwavelength Raman polarization and water-vapor lidar Polly^{XT}: the neXT
1402 generation, *Atmos. Meas. Tech.*, 9, 1767–1784, <https://doi.org/10.5194/amt-9-1767-2016>, 2016.

1403
1404 Errera, Q., Y. Bennouna, M. Schulz, H.J. Eskes, S. Basart, A. Benedictow, A.-M. Blechschmidt, S.
1405 Chabriat, H. Clark, E. Cuevas, H. Flentje, K.M. Hansen, U. Im, J. Kapsomenakis, B. Langerock, K.
1406 Petersen, A. Richter, N. Sudarchikova, V. Thouret, A. Wagner, Y. Wang, T. Warneke, C. Zerefos,
1407 Validation report of the CAMS global Reanalysis of aerosols and reactive gases, years 2003–2020,

1408 Copernicus Atmosphere Monitoring Service (CAMS) report, CAMS84_2018SC3_D5.1.1-2020.pdf,
1409 June 2021, doi:10.24380/8gf9-k005.

1410 European Space Agency (ESA): The four candidate Earth explorer core missions: Atmospheric
1411 dynamics mission, ESA Report for Mission Selection ESA SP, 1233, 145 pp., 1999

1412

1413 European Space Agency (ESA): ADM-Aeolus Science Report, ESA SP-1311, 121 pp., available at:
1414 <https://earth.esa.int/documents/10174/1590943/AEOL002.pdf> (last access: 14 June 2022), 2008.

1415

1416 European Space Agency (ESA): “ADM-Aeolus Mission Requirements Document”, ESA EOP-
1417 SM/2047, 57 pp., available at: http://esamultimedia.esa.int/docs/EarthObservation/ADM-Aeolus_MRD.pdf (last access: 2 November 2019), 2016.

1419

1420 Fernald, F. G.: Analysis of atmospheric lidar observations: some comments, Appl. Opt., 23, 652–653,
1421 doi.org/10.1364/AO.23.000652, 1984.

1422

1423 Flamant, P., Dabas, A., Martinet, P., Lever, V., Flament, T., Trapon, D., Olivier, M., Cuesta, J., and
1424 Huber, D.: Aeolus L2A Algorithm Theoretical Baseline Document, Particle optical properties
1425 product, version 5.7, available at: <https://earth.esa.int/eogateway/catalog/aeolus-l2a-aerosol-cloud-optical-product> (last access: 14 December 2021), 2021.

1427

1428 Flament, T., Trapon, D., Lacour, A., Dabas, A., Ehlers, F., and Huber, D.: Aeolus L2A aerosol optical
1429 properties product: standard correct algorithm and Mie correct algorithm, Atmos. Meas. Tech., 14,
1430 7851–7871, <https://doi.org/10.5194/amt-14-7851-2021>, 2021.

1431

1432 Fountoulakis, I., Papachristopoulou, K., Proestakis, E., Gkikas, A., Ioannis Raptis, P., Siomos, N.,
1433 Kontoes, C., and Kazadzis, S.: Effect of aerosol vertical distribution on the transfer of solar radiation
1434 through the atmosphere, EGU21-6111, <https://doi.org/10.5194/egusphere-egu21-6111>, 2021.

1435

1436 Freudenthaler, V.: About the effects of polarising optics on lidar signals and the $\Delta 90$ calibration,
1437 Atmos. Meas. Tech., 9, 4181–4255, <https://doi.org/10.5194/amt-9-4181-2016>, 2016.

1438

1439 Freudenthaler, V., Linné, H., Chaikovski, A., Rabus, D., Groß, S.: EARLINET lidar quality assurance
1440 tools, Atmos. Chem. Phys. Discuss., <https://doi.org/10.5194/amt-2017-395>, 2018.

1441

1442 Gelaro, R., McCarty, W., Suárez, M. J., Todling, R., Molod, A., Takacs, L., Randles, C. A., Darmenov,
1443 A., Bosilovich, M. G., Reichle, R., Wargan, K., Coy, L., Cullather, R., Draper, C., Akella, S.,
1444 Buchard, V., Conaty, A., da Silva, A. M., Gu, W., Kim, G., Koster, R., Lucchesi, R., Merkova, D.,
1445 Nielsen, J. E., Partyka, G., Pawson, S., Putman, W., Riendecker, M., Schubert, S. D., Sienkiewicz, M.,
1446 and Zhao, B.: The Modern-Era Retrospective Analysis for Research and Applications, Version 2
1447 (MERRA-2), *J. Climate*, 30, 5419–5454, <https://doi.org/10.1175/JCLI-D-16-0758.1>, 2017.

1448

1449 Gerasopoulos, E., Andreae, M. O., Zerefos, C. S., Andreae, T. W., Balis, D., Formenti, P., Merlet, P.,
1450 Amiridis, V., and Papastefanou, C.: Climatological aspects of aerosol optical properties in Northern
1451 Greece, *Atmos. Chem. Phys.*, 3, 2025–2041, <https://doi.org/10.5194/acp-3-2025-2003>, 2003.

1452

1453 Gerasopoulos, E., Amiridis, V., Kazadzis, S., Kokkalis, P., Eleftheratos, K., Andreae, M. O., Andreae,
1454 T. W., El-Askary, H., and Zerefos, C. S.: Three-year ground based measurements of aerosol optical
1455 depth over the Eastern Mediterranean: the urban environment of Athens, *Atmos. Chem. Phys.*, 11,
1456 2145–2159, <https://doi.org/10.5194/acp-11-2145-2011>, 2011.

1457

1458 Gialitaki, A., Tsekeli, A., Amiridis, V., Ceolato, R., Paulien, L., Kampouri, A., Gkikas, A., Solomos,
1459 S., Marinou, E., Haarig, M., Baars, H., Ansmann, A., Lapyonok, T., Lopatin, A., Dubovik, O., Groß,
1460 S., Wirth, M., Tsichla, M., Tsikoudi, I., and Balis, D.: Is the near-spherical shape the “new black” for
1461 smoke?, *Atmos. Chem. Phys.*, 20, 14005–14021, <https://doi.org/10.5194/acp-20-14005-2020>, 2020.

1462

1463 Giles, D. M., Sinyuk, A., Sorokin, M. G., Schafer, J. S., Smirnov, A., Slutsker, I., Eck, T. F., Holben,
1464 B. N., Lewis, J. R., Campbell, J. R., Welton, E. J., Korkin, S. V., and Lyapustin, A. I.: Advancements
1465 in the Aerosol Robotic Network (AERONET) Version 3 database – automated near-real-time quality
1466 control algorithm with improved cloud screening for Sun photometer aerosol optical depth (AOD)
1467 measurements, *Atmos. Meas. Tech.*, 12, 169–209, <https://doi.org/10.5194/amt-12-169-2019>, 2019.

1468

1469 Gkikas, A., Hatzianastassiou, N., Mihalopoulos, N., Katsoulis, V., Kazadzis, S., Pey, J., Querol, X.,
1470 and Torres, O.: The regime of intense desert dust episodes in the Mediterranean based on
1471 contemporary satellite observations and ground measurements, *Atmos. Chem. Phys.*, 13, 12135–
1472 12154, <https://doi.org/10.5194/acp-13-12135-2013>, 2013.

1473

Formatted: Font: (Default) Times New Roman, 12 pt

- 1474 Gkikas, A., Houssos, E. E., Lolis, C. J., Bartzokas, A., Mihalopoulos, N., and Hatzianastassiou, N.:
1475 Atmospheric circulation evolution related to desert-dust episodes over the Mediterranean, *Q. J. Roy.*
1476 *Meteor. Soc.*, 141, 1634–1645, <https://doi.org/10.1002/qj.2466>, 2015.
- 1477
- 1478 Gkikas, A., Basart, S., Hatzianastassiou, N., Marinou, E., Amiridis, V., Kazadzis, S., Pey, J., Querol,
1479 X., Jorba, O., Gassó, S., and Baldasano, J. M.: Mediterranean intense desert dust outbreaks and their
1480 vertical structure based on remote sensing data, *Atmos. Chem. Phys.*, 16, 8609–8642,
1481 <https://doi.org/10.5194/acp-16-8609-2016>, 2016.
- 1482
- 1483 Gkikas, A., Obiso, V., Pérez García-Pando, C., Jorba, O., Hatzianastassiou, N., Vendrell, L., Basart,
1484 S., Solomos, S., Gassó, S., and Baldasano, J. M.: Direct radiative effects during intense Mediterranean
1485 desert dust outbreaks, *Atmos. Chem. Phys.*, 18, 8757–8787, <https://doi.org/10.5194/acp-18-8757-2018>, 2018.
- 1486
- 1487
- 1488 Gkikas, A., Proestakis, E., Amiridis, V., Kazadzis, S., Di Tomaso, E., Marinou, E., Hatzianastassiou,
1489 N., Kok, J. F., and García-Pando, C. P.: Quantification of the dust optical depth across spatiotemporal
1490 scales with the MIDAS global dataset (2003–2017), *Atmos. Chem. Phys.*, 22, 3553–3578,
1491 <https://doi.org/10.5194/acp-22-3553-2022>, 2022.
- 1492
- 1493 Gueymard, C. A. and Yang, D.: Worldwide validation of CAMS and MERRA-2 reanalysis aerosol
1494 optical depth products using 15 years of AERONET observations, *Atmos. Environ.*, 225, 117216,
1495 <https://doi.org/10.1016/j.atmosenv.2019.117216>, 2020.
- 1496
- 1497 Haywood, J. M., Abel, S. J., Barrett, P. A., Bellouin, N., Blyth, A., Bower, K. N., Brooks, M.,
1498 Carslaw, K., Che, H., Coe, H., Cotterell, M. I., Crawford, I., Cui, Z., Davies, N., Dingley, B., Field,
1499 P., Formenti, P., Gordon, H., de Graaf, M., Herbert, R., Johnson, B., Jones, A. C., Langridge, J. M.,
1500 Malavelle, F., Partridge, D. G., Peers, F., Redemann, J., Stier, P., Szpek, K., Taylor, J. W., Watson-
1501 Parris, D., Wood, R., Wu, H., and Zuidema, P.: The Cloud–Aerosol–Radiation Interaction and
1502 Forcing: Year 2017 (CLARIFY-2017) measurement campaign, *Atmos. Chem. Phys.*, 21, 1049–1084,
1503 <https://doi.org/10.5194/acp-21-1049-2021>, 2021.
- 1504
- 1505 Health Effects Institute, 2019, State of Global Air 2019, Special Report, Boston, MA: Health Effects
1506 Institute, ISSN 2578-6873,
1507 https://www.stateofglobalair.org/sites/default/files/soga_2019_report.pdf, 2019.

1508

1509 Horányi, A., Cardinali, C., Rennie, M., and Isaksen, L.: The assimilation of horizontal line-of-sight
1510 wind information into the ECMWF data assimilation and forecasting system. Part I: The assessment
1511 of wind impact, *Q. J. R. Meteorol. Soc.*, 141, 1223–1232, <https://doi.org/10.1002/qj.2430>, 2015a.

1512

1513 Horányi, A., Cardinali, C., Rennie, M., and Isaksen, L.: The assimilation of horizontal line-of-sight
1514 wind information into the ECMWF data assimilation and forecasting system. Part II: The impact of
1515 degraded wind observations, *Q. J. R. Meteorol. Soc.*, 141, 1233–1243,
1516 <https://doi.org/10.1002/qj.2551>, 2015b.

1517

1518 Illingworth, A. J., Barker, H. W., Beljaars, A., Ceccaldi, M., Chepfer, H., Clerbaux, N., Cole, J.,
1519 Delanoë, J., Domenech, C., Donovan, D. P., Fukuda, S., Hirakata, M., Hogan, R. J., Huenerbein, A.,
1520 Kollias, P., Kubota, T., Nakajima, T., Nakajima, T. Y., Nishizawa, T., Ohno, Y., Okamoto, H., Oki,
1521 R., Sato, K., Satoh, M., Shephard, M. W., Velázquez-Blázquez, A., Wandinger, U., Wehr, T., and
1522 van Zadelhoff, G.-J.: The EarthCARE Satellite: The Next Step Forward in Global Measurements of
1523 Clouds, Aerosols, Precipitation, and Radiation, *Bull. Amer. Meteor. Soc.*, 96, 1311–1332,
1524 <https://doi.org/10.1175/BAMS-D-12-00227.1>, 2015.

1525

1526 Inness, A., Ades, M., Agustí-Panareda, A., Barré, J., Benedictow, A., Blechschmidt, A.-M.,
1527 Dominguez, J. J., Engelen, R., Eskes, H., Flemming, J., Huijnen, V., Jones, L., Kipling, Z., Massart,
1528 S., Parrington, M., Peuch, V.-H., Razinger, M., Remy, S., Schulz, M., and Suttie, M.: The CAMS
1529 reanalysis of atmospheric composition, *Atmos. Chem. Phys.*, 19, 3515–3556,
1530 <https://doi.org/10.5194/acp-19-3515-2019>, 2019.

1531

1532 Isaksen, L. and Rennie, M.: A preliminary evaluation of using Aeolus L2B Winds in ECMWF's NWP
1533 system, with focus on the tropical region, in: *ESA Living Planet Symposium 2019*, Milan, Italy,
1534 <https://lps19.esa.int/NikalWebsitePortal/living-planet-symposium-2019/lps19/Agenda/AgendaItemDetail?id=64570099-bea7-4b8f-a54b-5b6ad81fa342>, last access: 8
1535 May 2020, 2019.

1537

1538 Jickells, T. D., An, Z. S., Andersen, K. K., Baker, A. R., Bergametti, G., Brooks, N., Cao, J. J., Boyd,
1539 P. W., Duce, R. A., Hunter, K. A., Kawahata, H., Kubilay, N., laRoche, J., Liss, P. S., Mahowald, N.,
1540 Prospero, J. M., Ridgwell, A. J., Tegen, I. and Torres, R.: Global Iron Connections Between Desert

1541 Dust, Ocean Biogeochemistry, and Climate, Science, 308(5718), 67–71,
1542 doi:10.1126/science.1105959, 2005.

1543

1544 Kampouri, A., Amiridis, V., Solomos, S., Gialitaki, A., Marinou, E., Spyrou, C., Georgoulias, A. K.,
1545 Akritidis, D., Papagiannopoulos, N., Mona, L., Scollo, S., Tsichla, M., Tsikoudi, I., Pytharoulis, I.,
1546 Karacostas, T., and Zanis, P.: Investigation of Volcanic Emissions in the Mediterranean: “The Etna–
1547 Antikythera Connection,” 12, 40, <https://doi.org/10.3390/atmos12010040>, 2021.

1548

1549 Kanakidou, M., Mihalopoulos, N., Kindap, T., Im, U., Vrekoussis, M., Gerasopoulos, E., Dermitzaki,
1550 E., Unal, A., Kocak, M., Markakis, K., Melas, D., Kouvarakis, G., Youssef, A. F., Richter, A.,
1551 Hatzianastassiou, N., Hilboll, A., Ebojie, F., Wittrock, F., von Savigny, C., Burrows, J. P.,
1552 Ladstaetter-Weissenmayer, A., and Moubasher, H.: Megacities as hot spots of air pollution in the East
1553 Mediterranean, *Atmos. Environ.*, 45, 1223–1235, <https://doi.org/10.1016/j.atmosenv.2010.11.048>,
1554 2011.

1555

1556 Kanitz, T., Lochard, J., Marshall, J., McGoldrick, P., Lecrenier, O., Bravetti, P., Reitebuch, O.,
1557 Rennie, M., Wernham, D., and Elfving, A.: Aeolus first light: first glimpse, in: International
1558 Conference on Space Optics – ICSO 2018, 9–12 October 2018, Chania, Greece, vol. 11180, 659–
1559 664, <https://doi.org/10.1117/12.2535982>, 2019.

1560

1561 Klett, J. D.: Stable analytical inversion solution for processing lidar returns, *Appl. Optics*, 20, 211–
1562 220, <https://doi.org/10.1364/AO.20.000211>, 1981.

1563

1564 Kosmopoulos, P. G., Kazadzis, S., El-Askary, H., Taylor, M., Gkikas, A., Proestakis, E., Kontois, C.
1565 and El-Khayat, M. M.: Earth-Observation-Based Estimation and Forecasting of Particulate Matter
1566 Impact on Solar Energy in Egypt, *Remote Sens.*, 10(12), 1870, doi:10.3390/rs10121870, 2018.

1567

1568 Kosmopoulos, P.G., Kazadzis, S., Taylor, M., Raptis, P.I., Keramitsoglou, I., Kiranoudis, C., and
1569 Bais, A.F.: Assessment of the surface solar irradiance derived from real-time modelling techniques
1570 and verification with ground-based measurements. *Atmos. Meas. Tech.*, 11, pp 907-924, DOI:
1571 10.5194/amt-11-907-2018, 2018.

1572

1573 Lee, L., Zhang, J., Reid, J. S., and Yorks, J. E.: Investigation of CATS aerosol products and
1574 application toward global diurnal variation of aerosols, *Atmos. Chem. Phys.*, 19, 12687–12707,
1575 <https://doi.org/10.5194/acp-19-12687-2019, 2019.>

Formatted: Font: (Default) Times New Roman, 12 pt

Formatted: Justified, Line spacing: 1.5 lines

1576
1577 Lelieveld, J., Berresheim, H., Borrmann, S., Crutzen, P. J., Dentener, F. J., Fischer, H., Feichter, J.,
1578 Flatau, P. J., Heland, J., Holzinger, R., Korrman, R., Lawrence, M. G., Levin, Z., Markowicz, K.
1579 M., Mihalopoulos, N., Minikin, A., Ramanathan, V., de Reus, M., Roelofs, G. J., Scheeren, H. A.,
1580 Sciare, J., Schlager, H., Schultz, M., Siegmund, P., Steil, B., Stephanou, E. G., Stier, P., Traub, M.,
1581 Warneke, C., Williams, J., and Ziereis, H.: Global Air Pollution Crossroads over the Mediterranean,
1582 *Science*, 298, 794–799, <https://doi.org/10.1126/science.1075457>, 2002.

Deleted: ¶

1583
1584 Lelieveld, J., Evans, J. S., Fnais, M., Giannadaki, D., and Pozzer, A.: The contribution of outdoor air
1585 pollution sources to premature mortality on a global scale, *Nature*, 525, 367–371,
1586 <https://doi.org/10.1038/nature15371>, 2015.

1587
1588 Levy, R. C., Mattoo, S., Munchak, L. A., Remer, L. A., Sayer, A. M., Patadia, F., and Hsu, N. C.:
1589 The Collection 6 MODIS aerosol products over land and ocean, *Atmos. Meas. Tech.*, 6, 2989–3034,
1590 <https://doi.org/10.5194/amt-6-2989-2013, 2013.>

1591
1592 Li, W., El-Askary, H., Quran, M. A., Proestakis, E., Garay, M. J., Kalashnikova, O. V., Amiridis,
1593 V., Gkikas, A., Marinou, E., Piechota, T., and Manikandan, K. P.: An Assessment of Atmospheric
1594 and Meteorological Factors Regulating Red Sea Phytoplankton Growth, *Remote Sens.*, 10, 673,
1595 <https://doi.org/10.3390/rs10050673, 2018.>

1596
1597 Li, J., Carlson, B.E., Yung, Y.L. et al. Scattering and absorbing aerosols in the climate system. *Nat
1598 Rev Earth Environ* 3, 363–379 (2022). <https://doi.org/10.1038/s43017-022-00296-7>

1599
1600 Liu, D., Wang, Z., Liu, Z., Winker, D., and Trepte, C.: A height resolved global view of dust aerosols
1601 from the first year CALIPSO lidar measurements, *J. Geophys. Res.-Atmos.*, 113, D16214,
1602 <https://doi.org/10.1029/2007JD009776, 2008.>

1603
1604 Liu, Z., Kar, J., Zeng, S., Tackett, J., Vaughan, M., Avery, M., Pelon, J., Getzewich, B., Lee, K.-P.,
1605 Magill, B., Omar, A., Lucker, P., Trepte, C., and Winker, D.: Discriminating between clouds and

1607 aerosols in the CALIOP version 4.1 data products, *Atmos. Meas. Tech.*, 12, 703–734,
1608 <https://doi.org/10.5194/amt-12-703-2019>, 2019.

1609

1610 Lux, O., Lemmerz, C., Weiler, F., Marksteiner, U., Witschas, B., Rahm, S., Geiß, A., and Reitebuch,
1611 O.: Intercomparison of wind observations from the European Space Agency's Aeolus satellite mission
1612 and the ALADIN Airborne Demonstrator, *Atmos. Meas. Tech.*, 13, 2075–2097,
1613 <https://doi.org/10.5194/amt-13-2075-2020>, 2020.

1614

1615 Lux, O., Lemmerz, C., Weiler, F., Marksteiner, U., Witschas, B., Rahm, S., Geiß, A., Schäfler, A.,
1616 and Reitebuch, O.: Retrieval improvements for the ALADIN Airborne Demonstrator in support of
1617 the Aeolus wind product validation, *Atmos. Meas. Tech.*, 15, 1303–1331,
1618 <https://doi.org/10.5194/amt-15-1303-2022>, 2022.

1619

1620 Mallios, S. A., Daskalopoulou, V., and Amiridis, V.: Orientation of non spherical prolate dust
1621 particles moving vertically in the Earth's atmosphere, *J. Aerosol Sci.*, 151, 105657,
1622 doi:<https://doi.org/10.1016/j.jaerosci.2020.105657>, 2021.

1623

1624 Marinou, E., Amiridis, V., Binietoglou, I., Tsikerdekis, A., Solomos, S., Proestakis, E., Konsta, D.,
1625 Papagiannopoulos, N., Tsekeli, A., Vlastou, G., Zanis, P., Balis, D., Wandinger, U. and Ansmann,
1626 A.: Three-dimensional evolution of Saharan dust transport towards Europe based on a 9-year
1627 EARLINET-optimized CALIPSO dataset, *Atmos. Chem. Phys.*, 17(9), 5893–5919, doi:10.5194/acp-
1628 17-5893-2017, 2017.

1629

1630 [Martin, A., Weissmann, M., Reitebuch, O., Rennie, M., Geiß, A., and Cress, A.: Validation of Aeolus](#)
1631 [winds using radiosonde observations and numerical weather prediction model equivalents, Atmos.](#)
1632 [Meas. Tech., 14, 2167–2183, https://doi.org/10.5194/amt-14-2167-2021, 2021.](#)

1633

1634 Matthias, V., Freudenthaler, V., Amodeo, A., Balin, I., Balis, D., Bösenberg, J., Chaikovsky, A.,
1635 Chourdakis, G., Comeron, A., Delaval, A., De Tomasi, F., Eixmann, R., Hågård, A., Komguem, L.,
1636 Kreipl, S., Matthey, R., Rizi, V., Rodrigues, J., Wandinger, U., and Wang, X.: Aerosol lidar
1637 intercomparison in the framework of the EARLINET project. 1. Instruments, *Appl. Opt.*, 43, 961–
1638 976, doi:10.1364/AO.43.000961, 2004.

1639

1640 Mattis, I., D'Amico, G., Baars, H., Amodeo, A., Madonna, F., and Iarlori, M.: EARLINET Single
1641 Calculus Chain – technical – Part 2: Calculation of optical products, *Atmos. Meas. Tech.*, 9, 3009–
1642 3029, <https://doi.org/10.5194/amt-9-3009-2016>, 2016.

1643
1644 McGill, M. J., Yorks, J. E., Scott, V. S., Kupchock, A. W., and Selmer, P. A.: The Cloud Aerosol
1645 Transport System (CATS): A technology demonstration on the International Space Station, *Proc.*
1646 *SPIE* 9612, Lidar Remote Sensing for Environmental Monitoring XV, 96120A,
1647 <https://doi.org/10.1117/12.2190841>, 2015.

1648
1649 MétéoFrance: Algorithm theoretical basis document for cloud products (CMa-PGE01 v3.2, CT-
1650 PGE02 v2.2 & CTTH-PGE03 v2.2), Technical Report SAF/NWC/CDOP/MFL/SCI/ATBD/01,
1651 Paris: MétéoFrance, 2013.

1652
1653 Middleton, N., Tozer, P., and Tozer, B.: Sand and dust storms: underrated natural hazards, *Disasters*,
1654 43, 390–409, <https://doi.org/10.1111/disa.12320>, 2018.

1655
1656 Mishchenko, M. I. and Hovenier, J. W.: Depolarization of light backscattered by randomly oriented
1657 nonspherical particles, *Opt. Lett.*, 20(12), 1356, doi:10.1364/OL.20.001356, 1995.

1658
1659 Müller, D., Ansmann, A., Mattis, I., Tesche, M., Wandinger, U., Althausen, D., & Pisani, G. (2007).
1660 Aerosol-type-dependent lidar ratios observed with raman lidar. *Journal of Geophysical Research*
1661 *Atmospheres*, 112(16) doi:10.1029/2006JD008292

1662
1663 Okin, G. S., Mahowald, N., Chadwick, O. A. and Artaxo, P.: Impact of desert dust on the
1664 biogeochemistry of phosphorus in terrestrial ecosystems, *Global Biogeochemical Cycles*, 18(2),
1665 doi:10.1029/2003GB002145, 2004.

1666
1667 O'Neill, N. T., Eck, T. F., Smirnov, A., Holben, B. N., and Thulasiraman, S.: Spectral discrimination
1668 of coarse and fine mode optical depth, J. Geophys. Res., 108, 4559–4573,
1669 [https://doi.org/10.1029/2002JD002975, 2003.](https://doi.org/10.1029/2002JD002975)

1670
1671 Papagiannopoulos, N., D'Amico, G., Gialitaki, A., Ajtai, N., Alados-Arboledas, L., Amodeo, A.,
1672 Amiridis, V., Baars, H., Balis, D., Binietoglou, I., Comerón, A., Dionisi, D., Falconieri, A., Fréville,
1673 P., Kampouri, A., Mattis, I., Mijić, Z., Molero, F., Papayannis, A., Pappalardo, G., Rodríguez-Gómez,

Formatted: Font: (Default) Times New Roman, 12 pt

Formatted: Justified, Line spacing: 1.5 lines

Deleted: ¶

1675 A., Solomos, S. and Mona, L.: An EARLINET early warning system for atmospheric aerosol aviation
1676 hazards, *Atmospheric Chemistry and Physics*, 20(18), 10775–10789, doi:<https://doi.org/10.5194/acp-20-10775-2020>, 2020.

1678
1679 Pappalardo, G., Amodeo, A., Apituley, A., Comeron, A., Freudenthaler, V., Linné, H., Ansmann, A.,
1680 Bösenberg, J., D'Amico, G., Mattis, I., Mona, L., Wandinger, U., Amiridis, V., Alados-Arboledas,
1681 L., Nicolae, D., and Wiegner, M.: EARLINET: towards an advanced sustainable European aerosol
1682 lidar network, *Atmos. Meas. Tech.*, 7, 2389–2409, <https://doi.org/10.5194/amt-7-2389-2014>, 2014.

1683
1684 Papayannis, A., Balis, D., Amiridis, V., Chourdakis, G., Tsaknakis, G., Zerefos, C., Castanho, A. D.
1685 A., Nickovic, S., Kazadzis, S., and Grabowski, J.: Measurements of Saharan dust aerosols over the
1686 Eastern Mediterranean using elastic backscatter-Raman lidar, spectrophotometric and satellite
1687 observations in the frame of the EARLINET project, *Atmos. Chem. Phys.*, 5, 2065–2079,
1688 <https://doi.org/10.5194/acp-5-2065-2005>, 2005.

1689
1690 Paschou, P., Siomos, N., Tsekeli, A., Louridas, A., Georgoussis, G., Freudenthaler, V., Binietoglou,
1691 I., Tsaknakis, G., Tavernarakis, A., Evangelatos, C., von Bismarck, J., Kanitz, T., Meleti, C.,
1692 Marinou, E., and Amiridis, V.: The eVe reference polarisation lidar system for Cal/Val of Aeolus
1693 L2A product, *Atmos. Meas. Tech. Discuss. [preprint]*, <https://doi.org/10.5194/amt-2021-268>, in
1694 review, 2021.

1695
1696 Pappalardo, G., Wandinger, U., Mona, L., Hiebsch, A., Mattis, I., Amodeo, A., Ansmann, A., Seifert,
1697 P., Linne, H., Apituley, A., Alados Arboledas, L., Balis, D., Chaikovsky, A., D'Amico, G., De
1698 Tomasi, F., Freudenthaler, V., Giannakaki, E., Giunta, A., Grigorov, I., Iarlori, M., Madonna, F.,
1699 Mamouri, R.-E., Nasti, L., Papayannis, A., Pietruczuk, A., Pujadas, M., Rizi, V., Rocadenbosch, F.,
1700 Russo, F., Schnell, F., Spinelli, N., Wang, X., and Wiegner, M.: EARLINET correlative
1701 measurements for CALIPSO: First intercomparison results, *J. Geophys. Res.*, 115, D00H19,
1702 doi:10.1029/2009JD012147, 2010.

1703
1704 Pappalardo, G., Amodeo, A., Apituley, A., Comeron, A., Freudenthaler, V., Linné, H., Ansmann, A.,
1705 Bösenberg, J., D'Amico, G., Mattis, I., Mona, L., Wandinger, U., Amiridis, V., Alados-Arboledas,
1706 L., Nicolae, D., and Wiegner, M.: EARLINET: towards an advanced sustainable European aerosol
1707 lidar network, *Atmos. Meas. Tech.*, 7, 2389–2409, <https://doi.org/10.5194/amt-7-2389-2014>, 2014.

1709 Pérez, C., Nickovic, S., Pejanovic, G., Baldasano, J. M., and Özsoy, E.: Interactive dust-radiation
1710 modeling: A step to improve weather forecasts, *J. Geophys. Res.*, 111, 1–17, 2006.

1711

1712 Pisso, I., Sollum, E., Grythe, H., Kristiansen, N.I., Cassiani, M., Eckhardt, S., Arnold, D., Morton,
1713 D., Thompson, R.L., Groot Zwaftink, C.D., Evangelou, N., Sodemann, H., Haimberger, L., Henne,
1714 S., Brunner, D., Burkhardt, J.F., Fouilloux, A., Brioude, J., Philipp, A., Seibert, P., and Stohl, A.:
1715 FLEXPART 10.4 (Version 10.4), *Geosci. Model Dev. Discuss.* Zenodo,
1716 <https://doi.org/10.5281/zenodo.3542278>, 2019.

1717

1718 Pöschl, U.: Atmospheric Aerosols: Composition, Transformation, Climate and Health Effects,
1719 ANGEW CHEM INT EDIT, 44, 7520-7540, 10.1002/anie.200501122, 2005.

1720

1721 Proestakis, E., Amiridis, V., Marinou, E., Georgoulias, A. K., Solomos, S., Kazadzis, S., Chimot, J.,
1722 Che, H., Alexandri, G., Binietoglou, I., Daskalopoulou, V., Kourtidis, K. A., de Leeuw, G. and
1723 Ronald, J. van der A.: Nine-year spatial and temporal evolution of desert dust aerosols over South
1724 and East Asia as revealed by CALIOP, *Atmos. Chem. Phys.*, 18(2), 1337–1362, doi:10.5194/acp-18-
1725 1337-2018, 2018.

1726

1727 Proestakis, E., Amiridis, V., Marinou, E., Binietoglou, I., Ansmann, A., Wandinger, U., Hofer, J.,
1728 Yorks, J., Nowottnick, E., Makhmudov, A., Papayannis, A., Pietruczuk, A., Gialitaki, A., Apituley,
1729 A., Szkop, A., Muñoz Porcar, C., Bortoli, D., Dionisi, D., Althausen, D., Mamali, D., Balis, D.,
1730 Nicolae, D., Tettoni, E., Liberti, G. L., Baars, H., Mattis, I., Stachlewska, I. S., Voudouri, K. A., Mona,
1731 L., Mylonaki, M., Perrone, M. R., Costa, M. J., Sicard, M., Papagiannopoulos, N., Siomos, N.,
1732 Burlizzi, P., Pauly, R., Engelmann, R., Abdullaev, S., and Pappalardo, G.: EARLINET evaluation of
1733 the CATS Level 2 aerosol backscatter coefficient product, *Atmos. Chem. Phys.*, 19, 11743–11764,
1734 <https://doi.org/10.5194/acp-19-11743-2019>, 2019.

1735

1736 Pye, H.O.T., Ward-Caviness, C.K., Murphy, B.N. et al. Secondary organic aerosol association with
1737 cardiorespiratory disease mortality in the United States. *Nat Commun* 12, 7215 (2021).
1738 <https://doi.org/10.1038/s41467-021-27484-1>

1739

1740 Randles, C. A., da Silva, A. M., Buchard, V., Colarco, P. R., Darmenov, A., Govindaraju, R.,
1741 Smirnov, A., Holben, B., Ferrare, R., Hair, J., Shinozuka, Y., Flynn, C. J., Randles, C. A., Silva, A.
1742 M. da, Buchard, V., Colarco, P. R., Darmenov, A., Govindaraju, R., Smirnov, A., Holben, B., Ferrare,

- 1743 R., Hair, J., Shinozuka, Y., and Flynn, C. J.: The MERRA-2 Aerosol Reanalysis, 1980 Onward. Part
1744 I: System Description and Data Assimilation Evaluation, *J. Climate*, 30, 6823–6850,
1745 <https://doi.org/10.1175/JCLI-D-16-0609.1>, 2017.
- 1746
- 1747 Reitebuch, O., Lemmerz, C., Lux, O., Marksteiner, U., Rahm, S., Weiler, F., Witschas, B., Meringer,
1748 M., Schmidt, K., Huber, D., Nikolaus, I., Geiss, A., Vaughan, M., Dabas, A., Flament, T., Stieglitz,
1749 H., Isaksen, L., Rennie, M., de Kloe, J., Marseille, G.-J., Stoffelen, A., Wernham, D., Kanitz, T.,
1750 Straume, A.-G., Fehr, T., von Bismarck, J., Floberghagen, R., and Par- rinello, T.: Initial Assessment
1751 of the Performance of the First Wind Lidar in Space on Aeolus, *EPJ Web Conf.*, 237, 01010,
1752 <https://doi.org/10.1051/epjconf/202023701010>, 2020.
- 1753
- 1754 Remer, L. A., Kleidman, R. G., Levy, R. C., Kaufman, Y. J., Tanré, D., Mattoo, S., Martins, J. V.,
1755 Ichoku, C., Koren, I., Yu, H. and Holben, B. N.: Global aerosol climatology from the MODIS satellite
1756 sensors, *J. Geophys. Res.-Atmos.*, 113, D14S07, <https://doi.org/10.1029/2007JD009661>, 2008.
- 1757
- 1758 Rennie, M. P. and Isaksen, L.: Investigations Into the Quality of Aeolus L2B Winds Using the
1759 ECMWF Model and Initial NWP Impact Assessment, in: *ESA Living Planet Symposium 2019*,
1760 Milan, Italy, <https://lps19.esa.int/NikalWebsitePortal/living-planet-symposium-2019/lps19/Agenda/AgendaItemDetail?id=1a3d272c-f7d1-4847-b1c4-08c452f9405f>, last access: 8
1761 May 2020, 2019.
- 1762
- 1763
- 1764 Rennie, M. P., Isaksen, L., Weiler, F., de Kloe, J., Kanitz, T., and Reitebuch, O.: The impact of Aeolus
1765 wind retrievals on ECMWF global weather forecasts, *Q. J. Roy. Meteor. Soc.*, 147, 3555–3586,
1766 <https://doi.org/10.1002/qj.4142>, 2021.
- 1767
- 1768 Richardson, S. C., Mytilinaios, M., Foskinis, R., Kyrou, C., Papayannis, A., Pyrri, I., Giannoutsou,
1769 E., and Adamakis, I. D. S.: Bioaerosol detection over Athens, Greece using the laser induced
1770 fluorescence technique, *Sci. Total Environ.*, 696, 133906,
1771 <https://doi.org/10.1016/j.scitotenv.2019.133906>, 2019.
- 1772
- 1773 Roebeling, R. A., Feijt, A. J., and Stamnes, P.: Cloud property retrievals for climate monitoring:
1774 implications of differences between SEVIRI on METEOSAT-8 and AVHRR on NOAA-17, *J.*
1775 *Geophys. Res.*, 111, 20210, <https://doi.org/10.1029/2005JD006990>, 2006.
- 1776

1777 Roy, G. and Roy, N.: Relation between circular and linear depolarization ratios under multiple-
1778 scattering conditions, *Appl. Opt.*, doi:10.1364/ao.47.006563, 2008.

1779

1780 Sasano, Y. and Nakane, H.: Significance of the extinction/backscatter ratio and the boundary value
1781 term in the solution for the two-component lidar equation, *Appl. Opt.*, 23(1), 11_1--13,
1782 doi:10.1364/AO.23.0011_1, 1984.

1783

1784 Sayer, A. M., Hsu, N. C., Bettenhausen, C., and Jeong, M.-J.: Validation and uncertainty estimates
1785 for MODIS Collection 6 “Deep Blue” aerosol data, *J. Geophys. Res.*, 118, 7864–7873,
1786 <https://doi.org/10.1002/jgrd.50600>, 2013.

1787

1788 Schmetz, J., Pili, P., Tjemkes, S., Just, D., Kerkmann, J., Rota, S., and Ratier, A.: An introduction to
1789 Meteosat Second Generation (MSG), *B. Am. Meteorol. Soc.*, 83, 977–992,
1790 [https://doi.org/10.1175/1520-0477\(2002\)083<0977:AITMSG>2.3.CO;2](https://doi.org/10.1175/1520-0477(2002)083<0977:AITMSG>2.3.CO;2), 2002.

1791

1792 [Shinozuka, Y. and Redemann, J.: Horizontal variability of aerosol optical depth observed during the](#)
1793 [ARCTAS airborne experiment, *Atmos. Chem. Phys.*, 11, 8489–8495, <https://doi.org/10.5194/acp-11-8489-2011>, 2011.](#)
1794

1795

1796 Sinyuk, A., Holben, B. N., Eck, T. F., Giles, D. M., Slutsker, I., Korkin, S., Schafer, J. S., Smirnov,
1797 A., Sorokin, M., and Lyapustin, A.: The AERONET Version 3 aerosol retrieval algorithm, associated
1798 uncertainties and comparisons to Version 2, *Atmos. Meas. Tech.*, 13, 3375–3411,
1799 <https://doi.org/10.5194/amt-13-3375-2020>, 2020.

1800

1801 Siomos, N., Balis, D. S., Voudouri, K. A., Giannakaki, E., Filioglou, M., Amiridis, V., Papayannis,
1802 A., and Fragkos, K.: Are EARLINET and AERONET climatologies consistent? The case of
1803 Thessaloniki, Greece, *Atmos. Chem. Phys.*, 18, 11885–11903, <https://doi.org/10.5194/acp-18-11885-2018>, 2018.

1805

1806 Solomon S., Dube K., Stone K., Yu P., Kinnison D., Toon O.B., Strahan S.E., Rosenlof K.H.,
1807 Portmann R., Davis S., Randel W., Bernath P., Boone C., Bardeen C.G., Bourassa A., Zawada D.,
1808 Degenstein D.: On the stratospheric chemistry of midlatitude wildfire smoke (2022) *Proceedings of*
1809 *the National Academy of Sciences of the United States of America*, 119 (10), pp. e2117325119 DOI:
1810 10.1073/pnas.2117325119

- 1811
1812 Stoffelen, A., Pailleux, J., Källén, E., Vaughan, J. M., Isaksen, L., Flamant, P., Wergen, W.,
1813 Andersson, E., Schyberg, H., Culoma, A., Meynart, R., Endemann, M., and Ingmann, P.: The
1814 atmospheric dynamics mission for global wind field measurement, *B. Am. Meteorol. Soc.*, 86, 73-87,
1815 <https://doi.org/10.1175/BAMS-86-1-73>, 2005.
- 1816
1817 Stohl, A., Forster, C., Frank, A., Seibert, P., and Wotawa, G.: Technical note: The Lagrangian particle
1818 dispersion model FLEXPART version 6.2, *Atmos. Chem. Phys.*, 5, 2461–2474, doi:10.5194/acp-5-
1819 2461-2005, 2005.
- 1820
1821 Straume, A.G., Schuettemeyer, D., von Bismarck, J., Kanitz, T., Fehr, T., EOP-SM/2945/AGS-agb,
1822 PL-Plan, European Space Agency (ESA),
1823 <https://earth.esa.int/eogateway/documents/20142/1564626/Aeolus-Scientific-CAL-VAL-Implementation-Plan.pdf>, 2019.
- 1824
1825 Straume, A. G., Rennie, M., Isaksen, L., de Kloe, J., Marseille, G.-J., Stoffelen, A., Flament, T.,
1826 Stieglitz, H., Dabas, A., Huber, D., Reitebuch, O., Lemmerz, C., Lux, O., Marksteiner, U., Weiler,
1827 F., Witschas, B., Meringer, M., Schmidt, K., Nikolaus, I., Geiß, A., Flamant, P., Kanitz, T., Wernham,
1828 D., von Bismarck, J., Bley, S., Fehr, T., Floberghagen, R., and Parrinello, T.: ESA's space-based
1829 Doppler wind lidar mission Aeolus – First wind and aerosol product assessment results, *EPJ Web
1830 Conf.*, 237, 01007, <https://doi.org/10.1051/epjconf/202023701007>, 2020.
- 1831
1832 Tyrlis, E. and Lelieveld, J.: Climatology and Dynamics of the Summer Etesian Winds over the
1833 Eastern Mediterranean, *J. Atmos. Sci.*, 70, 3374–3396, 2013.
- 1834
1835 van der Werf, G. R., Randerson, J. T., Giglio, L., van Leeuwen, T. T., Chen, Y., Rogers, B. M., Mu,
1836 M., van Marle, M. J. E., Morton, D. C., Collatz, G. J., Yokelson, R. J., and Kasibhatla, P. S.: Global
1837 fire emissions estimates during 1997–2016, *Earth Syst. Sci. Data*, 9, 697–720,
1838 <https://doi.org/10.5194/essd-9-697-2017>, 2017.
- 1839
1840 Ulanowski, Z., Bailey, J., Lucas, P. W., Hough, J. H., and Hirst, E.: Alignment of atmospheric mineral
1841 dust due to electric field, *Atmos. Chem. Phys.*, 7, 6161–6173, <https://doi.org/10.5194/acp-7-6161-2007>, 2007.
- 1842
1843
1844

1845 Varlas, G.; Marinou, E.; Gialitaki, A.; Siomos, N.; Tsarpalis, K.; Kalivitis, N.; Solomos, S.; Tsekeri,
1846 A.; Spyrou, C.; Tsichla, M.; Kampouri, A.; Vervatis, V.; Giannakaki, E.; Amiridis, V.; Mihalopoulos,
1847 N.; Papadopoulos, A.; Katsafados, P. Assessing Sea-State Effects on Sea-Salt Aerosol Modeling in
1848 the Lower Atmosphere Using Lidar and In-Situ Measurements. *Remote Sens.*, 13, 614.
1849 <https://doi.org/10.3390/rs13040614>, 2021.

1850

1851 Voudouri, K.A., Siomos, N., Michailidis, K., D'Amico, G., Mattis, I., Balis, D.: Consistency of the
1852 Single Calculus Chain optical products with archived measurements from an EARLINET lidar
1853 station, *Remote Sensing*. 2020; 12(23):3969. <https://doi.org/10.3390/rs12233969>, 2020.

1854

1855 Wei, J., Li, Z., Peng, Y., and Sun, L.: MODIS Collection 6.1 aerosol optical depth products over land
1856 and ocean: validation and comparison, *Atmos. Environ.*, 201, 428–440, 2019

1857

1858 Weiler, F., Rennie, M., Kanitz, T., Isaksen, L., Checa, E., de Kloe, J., Okunde, N., and Reitebuch, O.:
1859 Correction of wind bias for the lidar on board Aeolus using telescope temperatures, *Atmos. Meas.
1860 Tech.*, 14, 7167–7185, <https://doi.org/10.5194/amt-14-7167-2021>, 2021.

1861

1862 Weinzierl, B., Ansmann, A., Prospero, J. M., Althausen, D., Benker, N., Chouza, F., Dollner, M.,
1863 Farrell, D., Fomba, W. K., Freudenthaler, V., Gasteiger, J., Groß, S., Haarig, M., Heinold, B.,
1864 Kandler, K., Kristensen, T. B., Mayol-Bracero, O. L., Müller, T., Reitebuch, O., Sauer, D., Schäfer,
1865 A., Schepanski, K., Spanu, A., Tegen, I., Toledano, C. and Walser, A.: The Saharan Aerosol Long-
1866 Range Transport and Aerosol–Cloud-Interaction Experiment: Overview and Selected Highlights,
1867 *Bull. Amer. Meteor. Soc.*, 98(7), 1427–1451, doi:10.1175/BAMS-D-15-00142.1, 2016.

1868

1869 [Wilks, D.S. Statistical Methods in the Atmospheric Sciences, 4th ed.; Elsevier: Cambridge, MA, USA, 2019.](#)

1871

1872 Winker, D. M., Vaughan, M. A., Omar, A., Hu, Y., Powell, K. A., Liu, Z., Hunt, W. H. and Young,
1873 S. A.: Overview of the CALIPSO Mission and CALIOP Data Processing Algorithms, *J. Atmos.
1874 Ocean. Technol.*, 26(11), 2310–2323, doi:10.1175/2009JTECHA1281.1, 2009.

1875

1876 Witschas, B., Lemmerz, C., Geiß, A., Lux, O., Marksteiner, U., Rahm, S., Reitebuch, O., and Weiler,
1877 F.: First validation of Aeolus wind observations by airborne Doppler wind lidar measurements,
1878 *Atmos. Meas. Tech.*, 13, 2381–2396, <https://doi.org/10.5194/amt-13-2381-2020>, 2020.

Formatted: Font: (Default) Times New Roman, 12 pt

Formatted: Justified, Line spacing: 1.5 lines

Deleted: ¶

1880

1881 Witschas, B., Lemmerz, C., Lux, O., Marksteiner, U., Reitebuch, O., Weiler, F., Fabre, F., Dabas, A.,
1882 Flament, T., Huber, D., and Vaughan, M.: Spectral performance analysis of the Aeolus Fabry–Pérot
1883 and Fizeau interferometers during the first years of operation, *Atmos. Meas. Tech.*, 15, 1465–1489,
1884 <https://doi.org/10.5194/amt-15-1465-2022>, 2022.

1885

1886 Zeng, S., Vaughan, M., Liu, Z., Trepte, C., Kar, J., Omar, A., Winker, D., Lucke, P., Hu, Y.,
1887 Getzewich, B., and Avery, M.: Application of high-dimensional fuzzy k -means cluster analysis to
1888 CALIOP/CALIPSO version 4.1 cloud–aerosol discrimination, *Atmos. Meas. Tech.*, 12, 2261–2285,
1889 <https://doi.org/10.5194/amt-12-2261-2019>, 2019.

1890

1891 Zerefos, C., Nastas, P., Balis, D., Papayannis, A., Kelepertis, A., Kannelopoulou, E., Nikolakis, D.,
1892 Eleftheratos, C., Thomas, W., and Varotsos, C.: A complex study of Etna's volcanic plume from
1893 ground-based, in situ and space-borne observations, *International J. Remote Sens.*, 27, 1855–1864,
1894 <https://doi.org/10.1080/01431160500462154>, 2006.

1895

1896

1897

1898

1899

1900

1901

1902

1903

1904

1905

1906

1907

1908

1909

1910

1911

1912

1913

1914

1915

1916

1917

1918
1919
1920
1921
1922
1923
1924

1925 **Table 1:** Statistical metrics for the unfiltered (clouds plus aerosols) Aeolus L2A SCA and SCA mid-bin backscatter (in
1926 $Mm^{-1}sr^{-1}$) profiles at each PANACEA site.

Station	SCA					SCA_mid_bin				
	Counts	Bias	Rel. Bias (%)	R	RMSE	Counts	Bias	Rel. Bias (%)	R	RMSE
ANT	255	0.06	13.63	0.49	1.14	173	0.25	45.59	0.57	1.01
ATH	60	0.73	199.65	0.49	2.26	43	1.16	272.84	0.52	3.10
THE	222	0.83	185.16	0.34	2.60	140	1.10	224.65	0.32	2.19

Formatted: Superscript

Formatted: Superscript

Formatted: English (United States)

1927

1928 **Table 2:** As in Table 1 but for the filtered (only aerosols) Aeolus backscatter retrievals (in $Mm^{-1}sr^{-1}$).

Formatted: English (United States)

Station	SCA					SCA_mid_bin				
	Counts	Bias	Rel. Bias (%)	R	RMSE	Counts	Bias	Rel. Bias (%)	R	RMSE
ANT	94	-0.10	-26.57	0.55	0.78	57	0.06	13.35	0.86	0.43
ATH	12	1.08	483.36	0.75	3.33	9	0.73	312.67	0.82	1.41
THE	133	0.46	130.49	0.39	1.86	81	0.55	145.08	0.43	1.20

1929

1930

1931

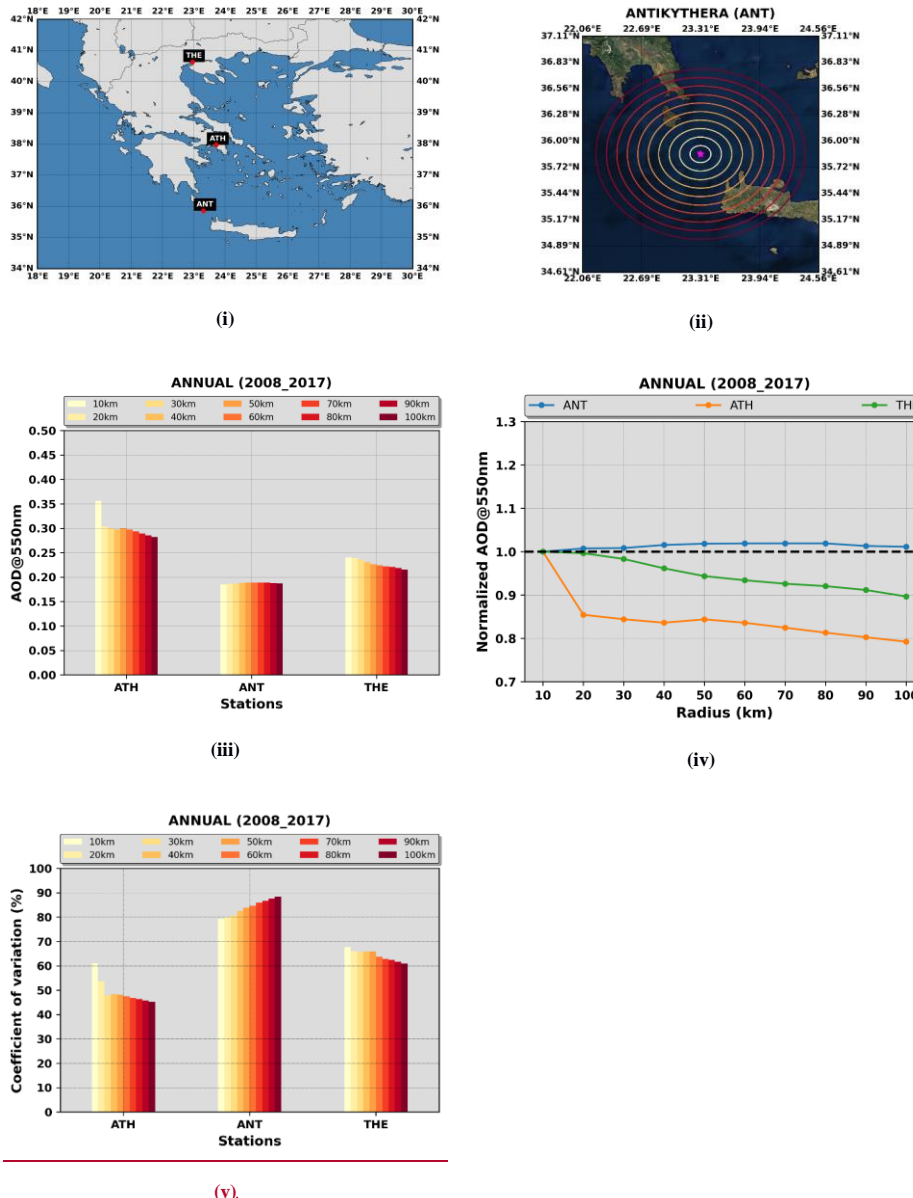
1932

1933

1934

1935

1936



Formatted: English (United States)

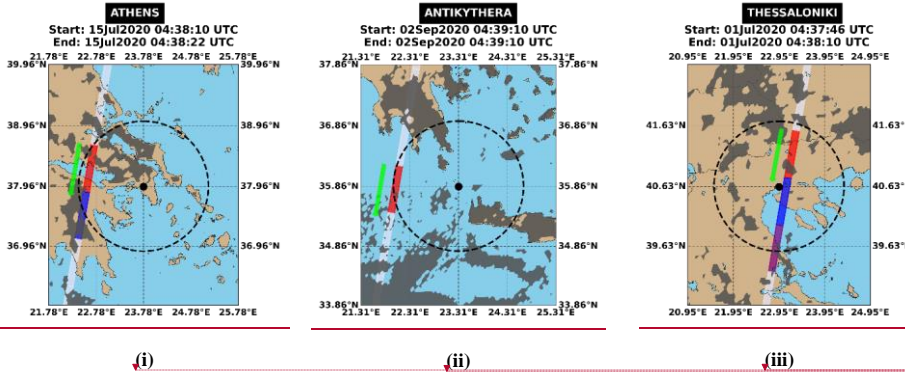
Deleted: ¶

¶

¶

¶

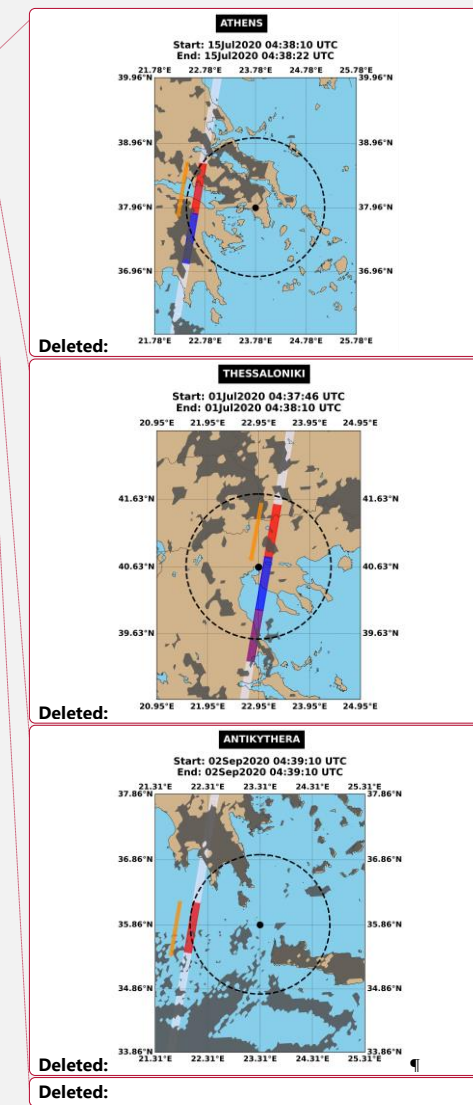
1937 **Figure 1:** (i) Locations of the three Greek PANACEA sites, namely Athens (ATH), Antikythera (ANT) and Thessaloniki (THE). (ii) Concentric circles, around the Antikythera island, of radii from 10 to 100 km with an incremental step of 10 km. (iii) Climatological MODIS-Aqua AOD levels, representative for the period 2008 – 2017, for each circle area centered at each PANACEA site. (iv) Normalized climatological AODs for each circle area with respect to the corresponding levels of the inner circle.



(i) (ii) (iii)

1948 **Figure 2:** The white stripe indicates the ALADIN's measurements track and the colored rectangles correspond to the
1949 Aeolus observations (~90 km along-track averaged measurements) falling within a radius of 120 km (dashed black line)
1950 of the PANACEA stations (black dot). The orange arrow shows the Aeolus flight directions (ascending or descending
1951 orbit). Dark grey shaded areas: MSG-SEVIRI cloud mask product (CLM) at the nearest time to Aeolus overpass. The
1952 start and end time (in UTC) of the ALADIN observations are given in the title of each plot.

1953
1954
1955
1956
1957
1958
1959
1960
1961
1962
1963
1964
1965
1966
1967
1968
1969
1970
1971
1972
1973



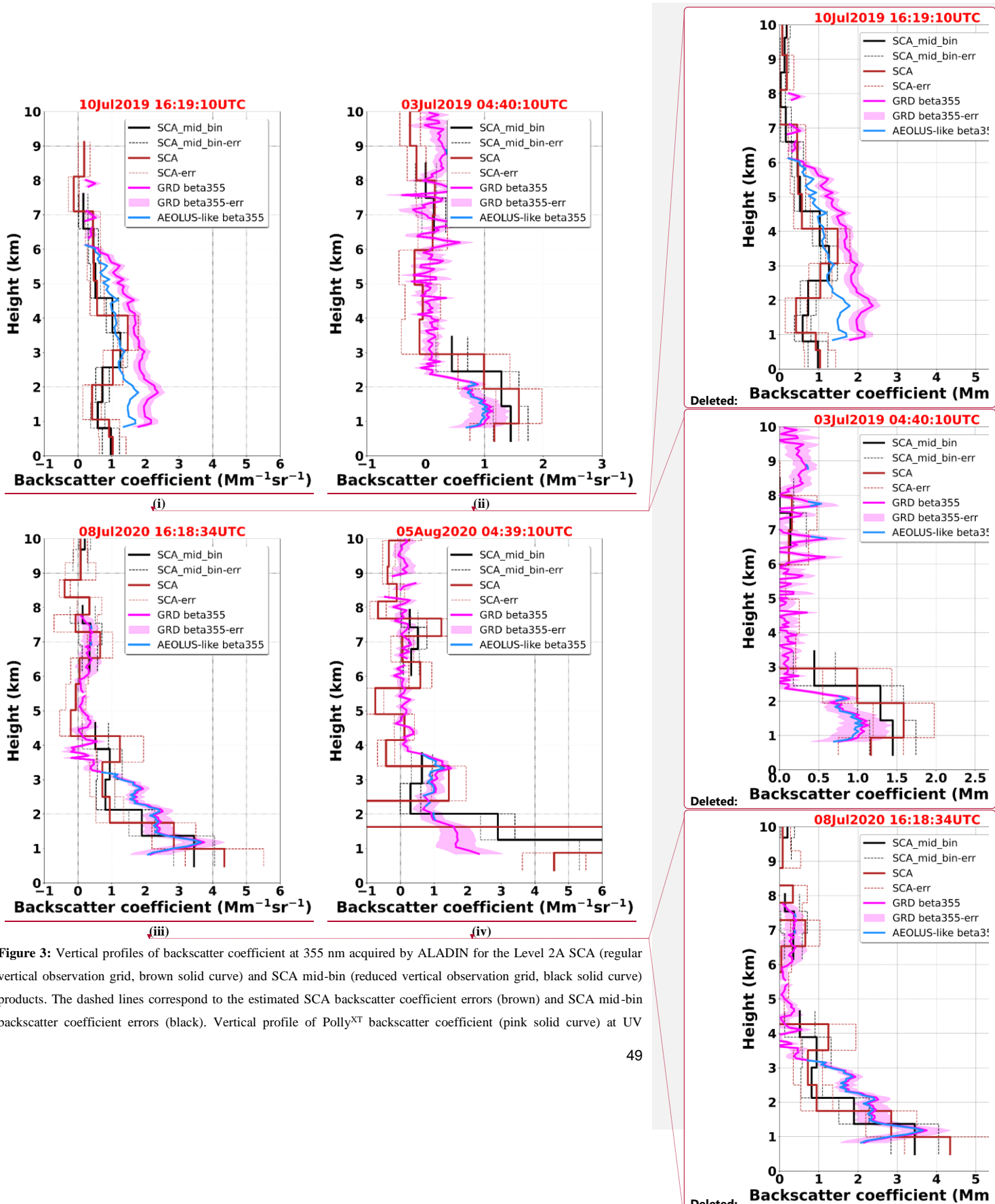
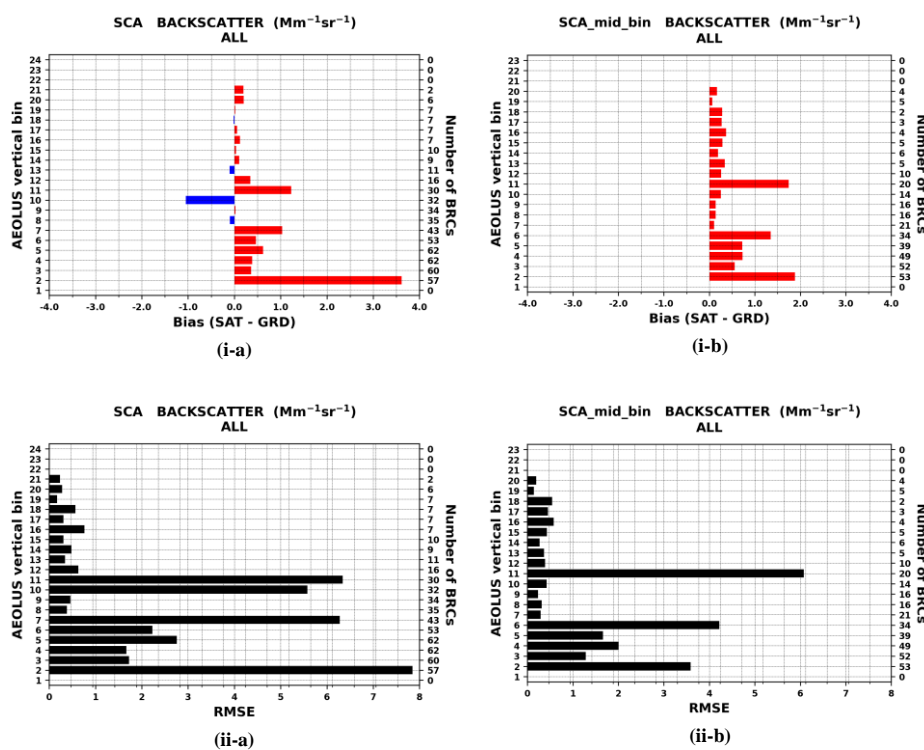
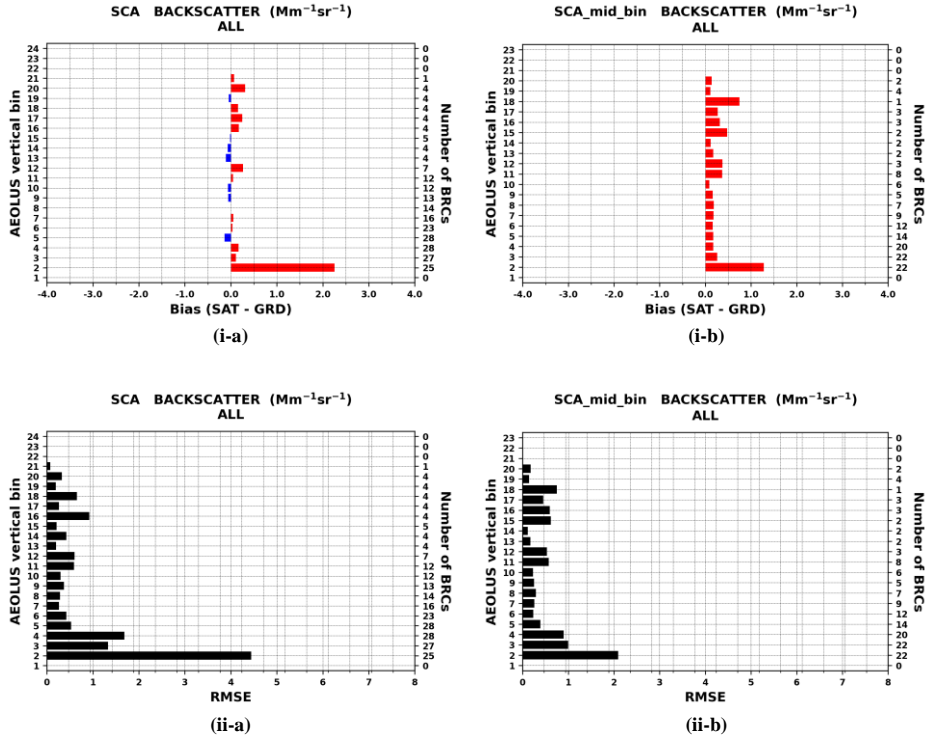


Figure 3: Vertical profiles of backscatter coefficient at 355 nm acquired by ALADIN for the Level 2A SCA (regular vertical observation grid, brown solid curve) and SCA mid-bin (reduced vertical observation grid, black solid curve) products. The dashed lines correspond to the estimated SCA backscatter coefficient errors (brown) and SCA mid-bin backscatter coefficient errors (black). Vertical profile of Polly^{XT} backscatter coefficient (pink solid curve) at UV

1990 wavelength (355 nm) and associated errors (pink shaded area). Polly^{XT} Aeolus-like backscatter coefficient (light-blue
1991 solid curve) after converting the linear-derived products to circular co-polar according to Paschou et al. (2021). The
1992 ground-based profiles have been acquired at the Antikythera station (southwest Greece) on: (i) 10th July 2019, (ii) 3rd July
1993 2019, (iii) 8th July 2020 and (iv) 5th August 2020. The red color font denotes which Aeolus BRC (along with the overpass
1994 time) has been selected based on the defined collocation criteria.
1995

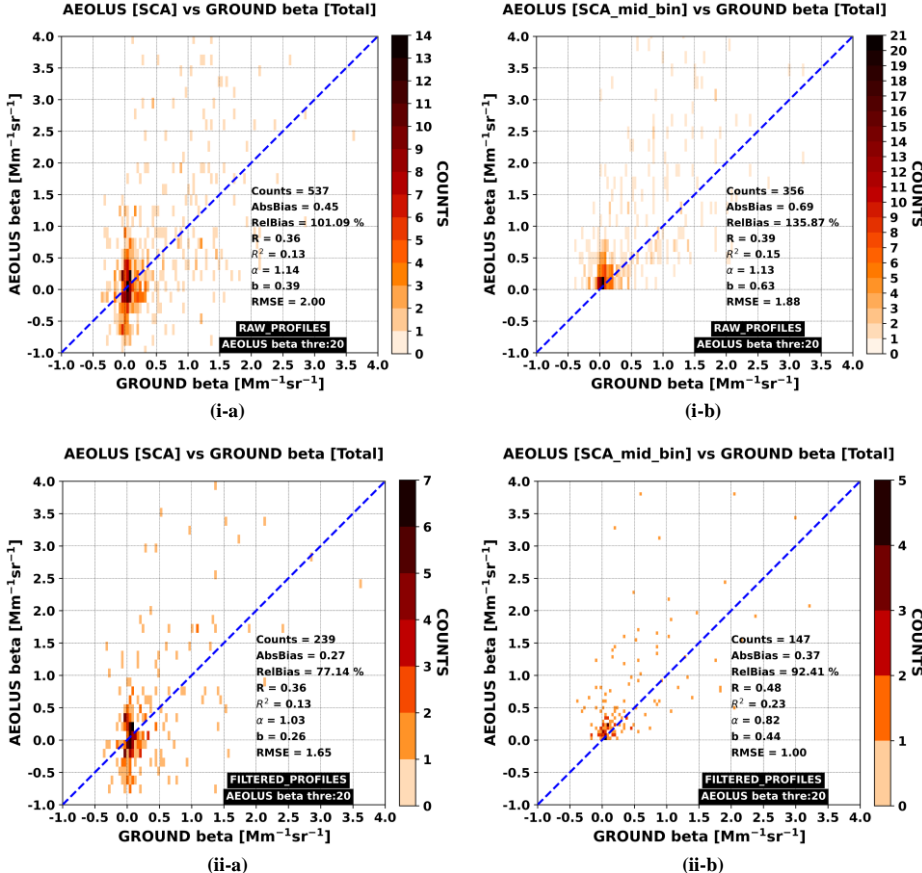


1996 **Figure 4:** Bias (i) and root mean square error (ii) metrics for the unfiltered Aeolus L2A backscatter retrievals reported at
1997 the regular (a) and mid-bin (b) vertical scales. The biases are defined as SAT-GRD and the positive/negative departures
1998 are depicted with red/blue bars. The statistical metrics are vertically resolved based on Aeolus bins indices (left y-axis).
1999 The number of BRCs participating in the metrics calculations at each bin are given on the right y-axis.
2000
2001
2002
2003
2004
2005
2006
2007
2008

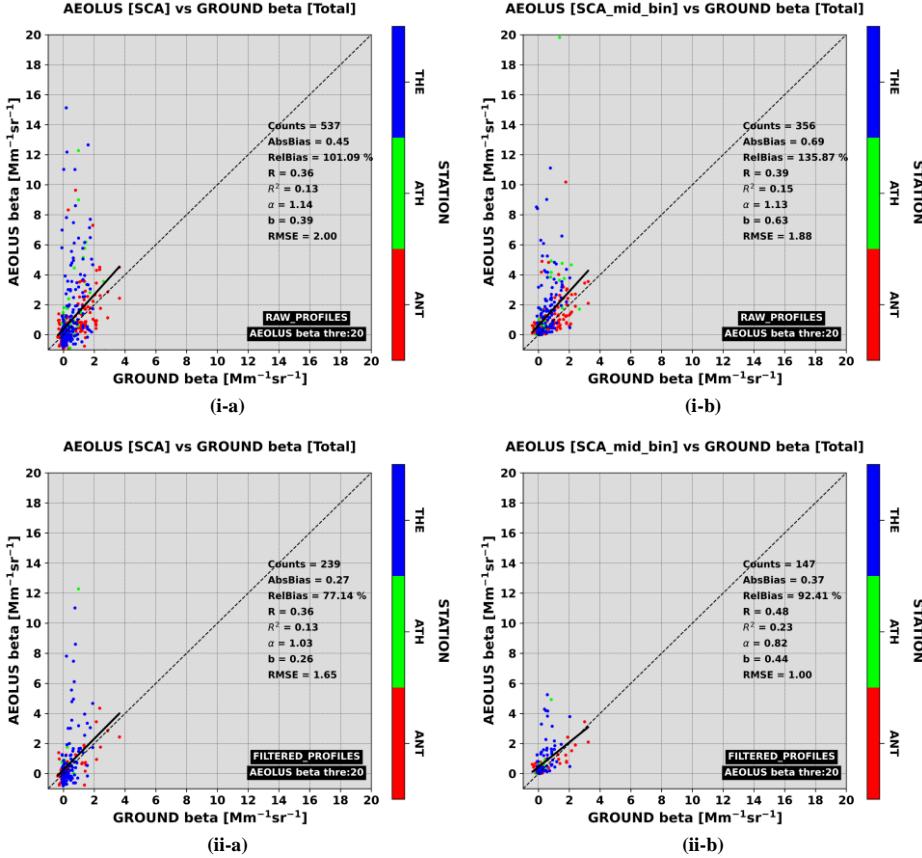


2009 **Figure 5:** As in Figure 4 but for the filtered Aeolus L2A backscatter retrievals.

2010
2011
2012
2013
2014
2015
2016
2017
2018
2019
2020
2021
2022
2023
2024
2025



2026 **Figure 6:** 2D histograms between Aeolus (y-axis) and ground-based (x-axis) backscatter coefficient retrievals. In the
2027 upper (i) and bottom (ii) panels are depicted the results for the cloud+aerosol backscatter (unfiltered) and cloud-cleared
2028 backscatter (filtered) Aeolus profiles, respectively. On the left and right columns are illustrated the results corresponding
2029 to Aeolus regular (24 bins) and mid-bin (23 bins) vertical scales, respectively. Aeolus backscatter values larger than 20
2030 $Mm^{-1} sr^{-1}$ are masked out from the collocated sample.



2035 **Figure 7:** Scatterplots between Aeolus (y-axis) and ground-based (x-axis) backscatter coefficient retrievals resolved
2036 based on the indices of Aeolus vertical bins (colored circles). In the upper (i) and bottom (ii) panels are depicted the
2037 results for the unfiltered and filtered Aeolus profiles, respectively. On the left and right columns are illustrated the results
2038 corresponding to Aeolus regular (24 bins) and mid-bin (23 bins) vertical scales, respectively. Aeolus backscatter values
2039 larger than $20 \text{ Mm}^{-1} \text{ sr}^{-1}$ are masked out from the collocated sample.

2040